Abstract

The potential for oil exploration on the Arctic Outer Continental Shelf warrants determination of an efficient method to clean up an oil spill. Traditional spill response equipment may not be practical in an Arctic environment; the presence of ice which may prevent proper deployment of equipment. The remoteness of the areas proposed for oil exploration lack the infrastructure and support networks necessary to stage a response to a large oil spill. These difficulties make it necessary to explore alternative means of oil spill cleanup. *In situ* burning is one method that may be particularly well-suited for arctic and sub-arctic environments due to the minimal amount of equipment required to achieve an efficient burn, i.e. high mass loss. The Arctic and sub-Arctic environments add an additional level of complexity by introducing a spill medium (ice) that is highly unstable at elevated temperatures. Our experiments sought to calculate the mass loss rate of oil mixtures to determine the efficiency with which they burn within ice channels of varying widths. Since fuel layer thickness is a critical factor in determining the effectiveness of an in situ burn the spread rate of oil along an ice channel was studied. Burning of oil in an ice channel yields low efficiencies (10%) primarily due to the geometric changes of the melting ice channel. The spreading was modeled as a constant flux rectilinear buoyancy-inertia governed flow. The melting causes an increase in the surface area and results in the critical thickness of the oil to be reached sooner. Based on the current bench-scale testing, losses due to ice melting cause the efficiencies of the burning process to be excessively low and not viable to full scale clean up. The results warrant future research to understand how varying other parameters, including starting mass of fuel, influence efficiencies.

Acknowledgments

It is a sincere pleasure for me to thank my advisors, Prof. Ali Rangwala and Prof. Morris Flynn who were able to guide me through this process. I appreciated the subtle efforts to look deeper into the problem and not be intimidated when looking into Pandora's box. I would like to thank Alyeska Pipeline Service Co. for partially funding the work presented in this document through their employee continuing education program. I must also thank Prof. Albert Simeoni who was able to provide me with a few last minute words of wisdom to carry me through to the end. I also am grateful for the help of Dr. Scott Pegau who participated as a reader. i also am appreciative of Al Allen's insight early on in the project. I need to thank Prof. Kathy Notarianni who provided me an ultimatum prior to my departure to Alaska "Finish or else". I want to also thank the students of the Combustion Lab, Brian Elias, Kulbhushan Joshi, Scott Rockwell and Yanxuan (Simon) Xi who assisted with my experimental setup and data collection. Without question I need to thank Emily Lescak who tolerated my many night and weekends of sitting in front of the computer instead of enjoying the great state of Alaska and for her editorial expertise. Parents must always be thanked, so I thank you both for instilling in me the motivation and mental fortitude to be where I am today.

Contents

List of Tables

List of Figures

Chapter 1

Introduction

Increased pressure to explore for and produce crude oil in the Arctic Outer Continental Shelf has prompted a critical analysis of the state-of-the-art of oil spill response techniques with respect to their applicability in Arctic and sub-Arctic regions. The primary hindrance to oil spill clean up in arctic waters is the presence of ice. Mechanical equipment can become choked with ice and may lead to low cleanup efficiencies. Once oil leaves containment, it can interact with ice in many different ways (Fig. 1.1) and as a consequence many different methods of spill response may be necessary. This has lead researchers to investigate alternative means of spill response that may be more suitable for arctic conditions; one of which includes *in situ* burning [1–10].

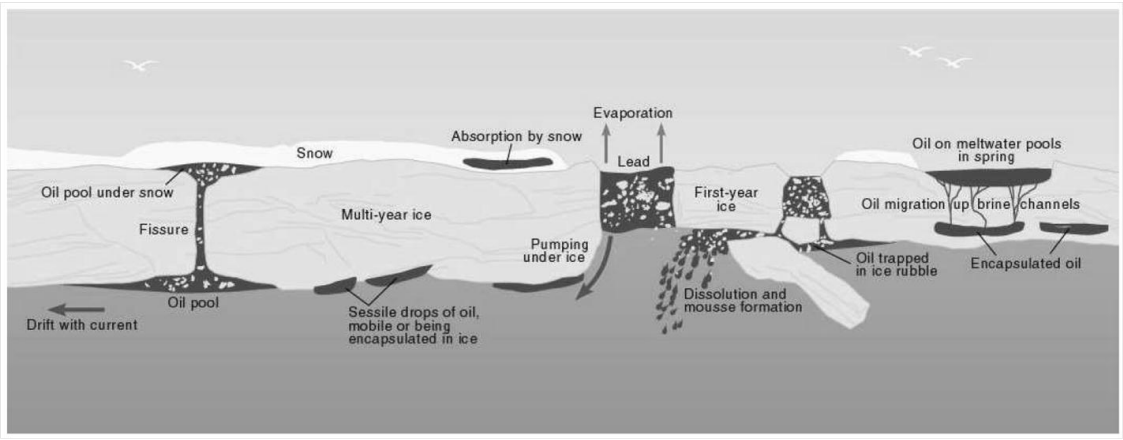

Figure 1.1: The far left side provides a visual description of the oil/ice interaction most applicable to this study [11]. If oil where to fill the cracks in the ice it could become difficult to remove with mechanical equipment. It is proposed that an *in situ* burn may allow the oil to rise out of the ice cracks and then be removed with a skimmer.

In situ burning is method of oil spill cleanup where the released oil is combusted directly on the spill

medium. This method is ideally suited for remote locations due to the relatively small amount of equipment and personnel required to achieve potentially high (99%) clean up efficiencies [10].The success of an *in situ* burn is highly dependent on the condition of the oil prior to ignition. Variables such as the degree of weathering, emulsifications and fuel layer depths all impact the efficacy of an *in situ* burn and can lead to varied success rates. As mentioned, the Arctic and sub-Arctic environments add an additional level of complexity by introducing a spill medium (ice) that is highly unstable at elevated temperatures. Oil released on solid ice may not be easily cleaned up due to the variable topography of an ice sheet. For this reason, we have chosen to perform a series of experiments which act to replicate oil spilled on solid ice by forming ice channels of varying widths in blocks of ice.

Due to concerns over air quality and the ability to safely ignite a large oil slick, *in situ* burning is not the preferred method for most oil spills [12, 13]. However, over the last 30 years, the *in situ* burning of crude oil spills has become a recognized and accepted method of oil spill cleanup with respect to the more conventional cleanup methods such as floating skimmers. Prior to the 1980s *in situ* burning was not considered a viable option due to a general lack of research as well as concerns over the environmental impact of burning oil in such large quantities. Researchers have since demonstrated that *in situ* burning is capable of achieving efficiencies of 99% under certain conditions and that the overall environmental impact of oil spill can be reduced due to the faster cleanup times[10]. *In situ* burning is a well suited option for Arctic operations where access is limited to ice roads and air transportation, ambient conditions commonly reach -40^o C and the polar night lasts 3 months. Additionally, *in situ* burning can have a high cleanup efficiency and relatively low post cleanup costs when compared with traditional means under these conditions.

Most *In situ* burning research has focused on open water burns while varying factors such as oil type, emulsification, degree of weathering (evaporation) and atmospheric conditions. A relatively small amount of published research has focused on oil spills in arctic conditions where percentage of ice cover and reduced temperatures are included as additional variables. [14, 15] This forms the motivation of the current study to explore *in situ* burning as an application to oil spill response in icy conditions. Experiments are performed using ice-channels of varying widths to measure mass loss rate when ignited. The mass loss rate data is used to analyze the variation in the critical thickness or the minimum thickness necessary for sustained ignition of the oil. It is shown that the dynamic environment created by the melting ice creates unique physical behavior unlike an oil slick burning on water. [16–19]

U.S. research evolved out of the need to develop response techniques after oil production on Alaska's North Slope increased. Norway has also made significant and notable contributions to oil spill research in Arctic waters as they too are an Arctic oil producing nation. [14, 15] As sea ice retreats more each summer the Arctic seaways will inevitably open up to commercial shipping traffic. This increased traffic augments

the potential for oil spills to occur as well as the need for more research on how to deal with spills in these conditions. Additionally, with increasing pressures to explore for oil in Alaska's Outer Continental Shelf (OCS), even more potential for oil spills in the presence of ice is possible. Many environmental organizations look at the lack of experience of oil spill response in the presence of ice as a major factor in their opposition to OCS development. The vast majority of offshore operations occur in temperate climates and as a result the oil spill response techniques are tailored to those conditions.

In situ burning research began in the late 1970's at Energetex Engineering. The earliest published research was conducted at the Environmental Protection Agency's Oil and Hazardous Materials Simulated Environmental Test Tank (OHMSETT) facility in Leonardo, New Jersey. A three part research project, conducted between 1984 and 1987, focused on burning of crude in varying ice concentrations in order to explore the range of conditions in which *in situ* burning is possible. The major conclusion of this preliminary study was that a 2.5 mm slick can sustain a burn on cold water and that the ice concentration and burn efficiencies are inversely related. [1–3]

After Smith and Diaz [1–3] concluded that *in situ* burning was a viable means of oil spill cleanup in arctic waters, research to further determine the parameters began in earnest. In 1986, Brown and Goodman [4] conducted twenty-five burns at the Esso Research ice basin in Calgary, Canada to study the effects of wind herding (the ability of the wind to push the slick), oil weathering, oil thickness and ice lead geometry of oil spills in lead ice and how these variables affected the minimum ignitable thickness.

They found that wind herding plays a significant role in the success of a burn and that even the effects of relatively low wind speeds are observable. Flame spread showed a linear relationship to wind speed with a dependence on weathering. Brash ice slowed flame spread and reduced wind herding effects and resulted in decreased efficiencies of up to 80%. The typical temperature rise in the water, 8 cm below the oil, was 5^o C approximately 1 minute after ignition and varied with the duration of the burn.

Buist and Dickins [5] conducted the first field research on *in situ* burning in 1987 Chedabucto Bay, Nova Scotia. Their purpose was to investigate the effects of dynamic ice conditions on oil spills and focus on the behavior of spills in ice. Using Fay's equation [20], they were able to accurately predicted the spread of oil between ice flows on the open water by correcting for oil viscosity at 0^o C. Using the ratio of density difference between water and oil to the density of water, as found in Fay's equation [20] $\frac{\rho_{water}-\rho_{oil}}{\rho_{water}}$, and ice concentration (by multiplying the calculated area by the fraction of the sea surface that was ice free) $R = (A_t \times \gamma)\,\pi^2$ where R is the radius of spill corrected for ice, A_t is the total area of the spill and γ is the fraction of sea surface free of ice, spread rates were able to be predicted. Additional observations were that the brash ice was an effective barrier for the oil spread and that the ice flow and oil slick drifted at the same rate.

Sveum et al., [6] as part of spill contingency plan for the Reindalen 1 drilling operation in Norway, researched *in situ* burning of oil spill in snow. Small scale tests yielded burn efficiencies of 90% to 99% for diesel and 90% to 98% for crude. It was noted that once the snow melted, the conditions mimiced oil on water *in situ* burning.

Bech [7] conducted a series of small and meso-scale experiments to determine the limits and efficiencies of *in situ* burning of water/oil emulsions, degree of evaporation and film thickness. The tests were conducted in 4 m^2 and 20 m^2 basins cut into fjord ice. He found that the efficiency of the burn decreased with both increasing emulsion and increased evaporation.

Guennette and Wighus [8] conducted a series of burns in basins in Spitsbergen, Norway in 1996. The purpose of the research was to study flame spreading across ice covered waters. This was the first experiment to take heat flux and heat load measurements for oil burns in ice were recorded. The maximum heat fluxes were measured 6.8 m off the surface at 400 kW/m^2.

In 2003, the Minerals Management Service (MMS) funded research to investigate the effects of waves on *in situ* burning of thin oil slicks in ice infested waters [10]. Their objective was to investigate the minimum ignitable thickness, combustion rate and residue amount as a result of waves on thin oil slicks burned *in situ* on frazil and brash ice. It was determined that in order for there to be ice remaining after a 3 mm thick slick burned, an ice depth of 5 mm was required and that the ignitable thickness varied with percent weathering and coverage. Brash ice proved to require the deepest minimum ignitable thickness.

Despite the research over the past 25 years, no study has publicly addressed the scenario of ice on a solid ice surface. The objective of this project was to understand how oil behavior on solid ice may affect an *in situ* burn. The research has been divided into four chapters. The first chapter being the introduction. The second chapter focuses on the mass loss rate of oil in an ice channel and has been accepted into the peer reviewed publication of the Combustion Institute's 34th International Symposium on Combustion. Chapter 2 is intended to evaluate the burning behavior of oil layer resting on ice by conducting a series of bench-scale tests. Since the roughness of sea ice can be highly varied, studying all possible combinations would be overly complex, so a single variable was chosen, channel width. The third chapter evaluates the effect of channel width on the spread rate and this chapter has been requested for review in the Journal of Loss Prevention in the Process Industries. Chapter 3 focuses on how channel width affects the transportation of the oil along an ice channel using the experimental configuration as determined in Chapter 2. The intent of having a similar experimental setup as found in Chapter 2 is to attempt to draw some conclusion between spread rates and mass loss rates. The overarching purpose of Chapter 3 is to recognize that an *in situ* burn does not occur immediately upon entering the environment and that some time lag must exist. It is hypothesized that a reduced channel width will negatively impact the mass loss rate while positively affecting the spreading rate.

Additionally, it is anticipated that the low surface temperature of the ice will negatively affect both the mass loss and spread rate. An iteration of this study was presented at the 2011 Mary Kay O'Connor Process Safety Center International Symposium.

Chapter 2

Mass Loss Rate

Introduction

The mass loss rate is an important parameter for the *in situ* burning of crude oil as it directly correlates to the efficacy of a burn with the presumption being that a low mass loss rate will be indicative of an inefficient combustion process. Combustion efficiencies of 99% have been achieved for crude oils in ice/water mixtures under test conditions [10]. Understanding how different environmental conditions impact the mass loss rate of a fuel layer can assist oil spill coordinators to determine if *in situ* burning techniques would be an effective option. A critical parameter of mass loss rate is the fuel layer's thickness. The critical thickness of a particular fuel will vary depending on many different physical properties, including flash point, heat of combustion, and thermal conductivity. A spill onto ice topography would create thicker fuel layers and should correspond to a more efficient combustion compared with an equivalent volume spill across an open body of water.

2.1 Methodology

To mimic an ice sheet an experimental apparatus was created (see Fig. 2.1) which used a 60 x 24 x 16 cm ice blocks with a channel of varying widths cut into the center. To study the effect of ice channel width on the mass loss rate three channel widths were used for the primary trials: 1 cm, 2 cm and 4 cm. Each channel was 40 cm long and 10 cm deep. Three trials at each width were conducted to form a data set of nine trials. The ice block was placed in a plastic tray which acted to capture any melted water, ensuring the mass loss that was recorded was from the lost oil and not melted water runoff; the loss due to water evaporation was assumed to be minimal and ignored. The unit was placed on top of a Setra Super II load cell that measured

mass with an accuracy of ±0.5 g. A thermocouple tree comprising of 7 type K thermocouples (0.125 cm diameter, spaced 2 cm apart) was placed in the center of the channel (Fig. 2.1b). The fuel consisted of a three parts SAE 30 motor oil [21] to one part petroleum ether [22]. This formed a homogeneous solution comprising of both high and low end volatiles and was intended to simulate a crude oil. The 3:1 oil solution was determined experimentally by burning a 100 ml mixture of motor oil and petroleum ether in an open stainless steel pan in the ambient such that a 99% burn efficiency could be achieved. Table 2.1 lists the relevant physical properties [21–23].

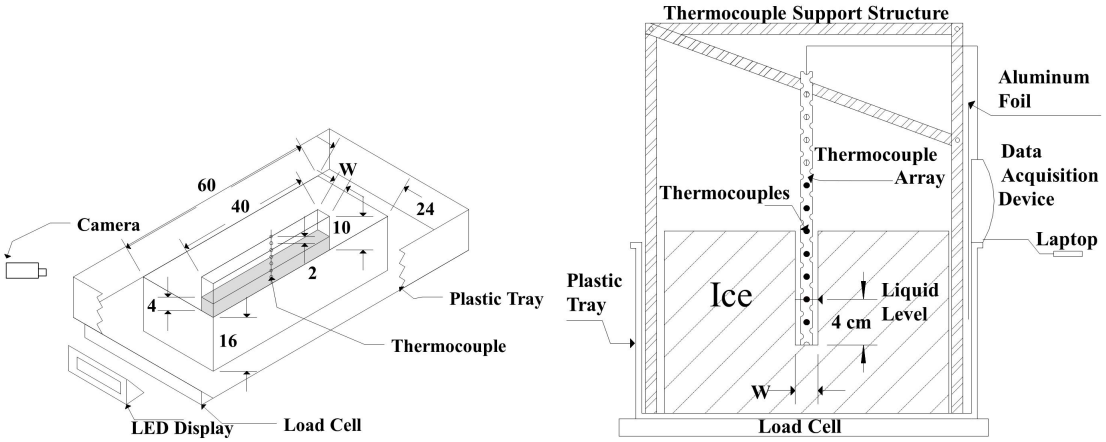

Figure 2.1: The 10 cm channel depth was chosen for the experimental setup based on the necessity to contain the oil within the ice channel. At depths less than 10 cm, there was a chance of overflowing the ice channel and allowing the fuel to flow into the containment area. The steel frame around the ice block was made of light gauge steel and allowed the equipment to be securely positioned near the ice block.

Table 2.1: Properties of Oil Mixture

Density	ρ	$844 kg/m^3$
Flash Point	T_{fp}	161^oC
Boiling Point	T_{bp}	236^oC
Thermal Conductivity	k	$0.146 W/m \cdot K$
Specific Heat	C_p	$1.912 J/kg \cdot K$
Thermal Diffusivity	α	$905 \times 10^{-7} m^2/s$

The quantity of oil poured into the ice cavity was adjusted to ensure that the initial thickness of the oil remained a constant for the three widths tested. This isolated the effects of the ice channel from the effects of fuel thickness. The experimental procedure comprised of pouring an oil layer (at initial temperature of 20 ^{o}C) in the ice cavity and igniting it immediately using a propane torch-igniter until a sustained flame was observed.

Two auxiliary tests were conducted in addition to the nine primary trials. One test used petroleum ether

in a 1 cm channel in order to verify the ease with which petroleum ether burns on ice. The second test used 300 ml of oil mixture in an aluminum-lined 4 cm ice channel. This test was performed to isolate the influence of the flows generated due to the melting water from the heat losses due to presence of ice on the burning behavior of the oil slick. All trials were allowed to burn to extinction except the petroleum ether which was stopped after 240 s because of flow over the sides of ice channel into the secondary containment.

2.2 Results and Discussion

As mentioned, three channel widths with similar length (40 cm) and fuel depth (nominally 3 cm in a channel depth of 10 cm) were ignited and the corresponding burning behavior of oil was analyzed. Measurements of the mass loss over time were taken at 1 second intervals and a 6th-order polynomial was fitted to the data. Figure 2.2 show the mass loss with respect to time of each trial; the data for all trials is located in Appendix A.

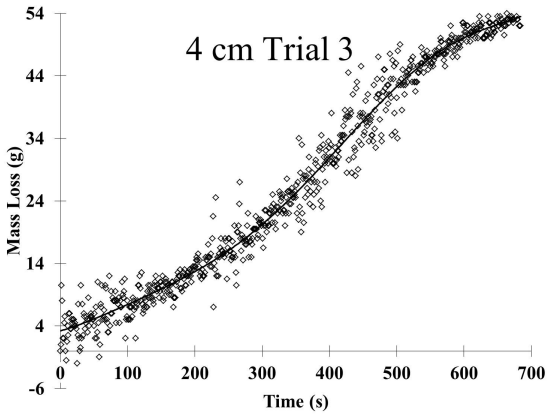

Figure 2.2: The raw data for the 4 cm channel width trial 3 is shown with a 6th-order polynomial trendline (Eq.2.1)

4 cm channel width trial 3 mass loss trendline equation

$$\begin{aligned} dM &= 6.1 \times 10^{-15} t^6 - 1.2 \times 10^{-11} t^5 + 7.4 \times 10^{-9} t^4 \\ &\quad - 1.9 \times 10^{-6} t^3 + 2.6 \times 10^{-4} t^2 + 2.9 \times 10^{-2} t + 3.2 \\ r^2 &= 0.98 \end{aligned} \tag{2.1}$$

2.2.1 Mass Loss Rate

Once the 6th order polynomial equation was obtained in could be differentiated to determine the rate of change in the mass with respect to time. The mass loss rate as a function of time is shown in Fig. 2.3,

2.4 and 2.5. The mass loss rate was found to be coupled to the dynamics of the channel (the melting of ice causing a change in the shape of the channel). Two zones were identified to characterize the burning behavior of an oil layer in the channel. The two zones are delineated using the peak mass loss rate. Zone 1 encompassed the period of the trial between the initial self-sustained flame and the peak mass loss rate. Initially, the trial is a deep ullage pool fire which burned inefficiently due to the limited availability of air. This is reflected in Fig. 2.3, 2.4 and 2.5 by a low initial mass loss rate. As each trial progressed, two effects coalesced to increase the mass loss rate as the flame melted away the channel wall. The first was the increase in the fuel's surface area and the second was the decrease in the ullage height. The second zone represents the period from the peak mass loss rate to extinction. Zone two was dominated by the critical fuel layer depth which, due to the changing fuel composition, is required to increase with time but was continually thinning due to the melting of the channel walls. The gray bars in Fig. 2.3, 2.4 and 2.5 represent the time span of milestone of the burn. The milestones being, ignition, peak mass loss rate and extinction.

The 1 cm and 2 cm trials have an initial period which corresponds to the time needed to achieve a self-sustaining flame based on intermittent piloted ignition. The mass loss rate is recorded from the time when a self-sustaining flame is visible through extinction and the effects of the ignition period are ignored. For this reason there is a period of time preceding the data in Fig. 2.3 and Fig. 2.4 which is represented as empty space. The time prior to ignition is shown to provide the reader with a sense of how long the oil was in contact with the ice before ignition occurred.

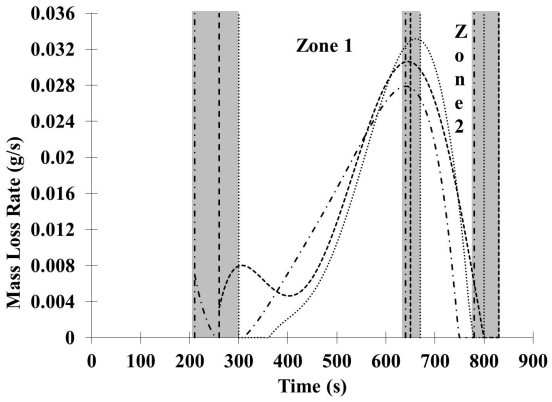

Figure 2.3: Equations 2.2, 2.3 and 2.4 provide the mass loss rate of the 1 cm channel width trials. The mass loss rates had a long period of negligible change in mass due to channel width prohibiting sufficient quantities of air reaching the flame. Eventually enough of the wall was melted to allow the flames to reach a peak mass loss rate.

$$\frac{dM}{dt} = -2.3 \times 10^{-14}t^5 + 2.8 \times 10^{-11}t^4 - 1.3 \times 10^{-8}t^3 + 3.1 \times 10^{-6}t^2 - 2.7 \times 10^{-4}t + 7.0 \times 10^{-3} \tag{2.2}$$

$$\frac{dM}{dt} = 3.1 \times 10^{-14}t^5 - 4.6 \times 10^{-11}t^4 + 2.2^{-8}t^3 - 3.9 \times 10^{-6}t^2 + 2.4 \times 10^{-4}t + 3.3 \times 10^{-3} \tag{2.3}$$

$$\frac{dM}{dt} = 2.1 \times 10^{-14}t^5 - 3.6^{-11}t^4 + 1.9^{-8}t^3 - 3.7 \times 10^{-6}t^2 + 3.5 \times 10^{-4}t - 1.2 \times 10^{-2} \tag{2.4}$$

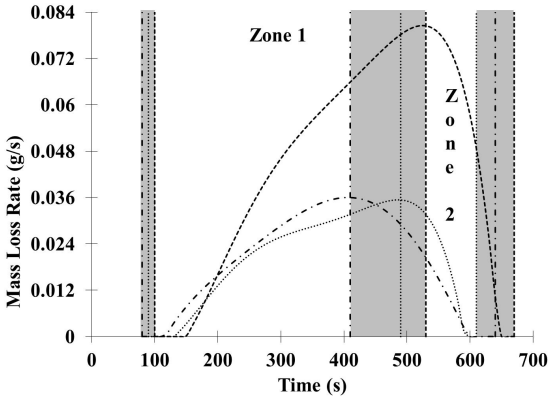

Figure 2.4: Equations 2.5, 2.6 and 2.7 are plotted to show the mass loss rate of the 2 cm channel width trials. Similar to, but shorter than the 1 cm channel width trials, a period of negligible mass loss exist due to deep ullage effects.

$$\frac{dM}{dt} = 1.7 \times 10^{-14}t^5 - 2.4 \times 10^{-11}t^4 + 1.2 \times 10^{-8}t^3 - 2.6 \times 10^{-6}t^2 + 4.2 \times 10^{-4}t - 1.2 \times 10^{-2} \tag{2.5}$$

$$\frac{dM}{dt} = -6.0 \times 10^{-14} * t^5 + 7.3 \times 10^{-11}t^4 - 3.2 \times 10^{-8}t^3 + 5.9 \times -6t^2 - 1.3 \times 10^{-4}t - 4.4 \times 10^{-3} \tag{2.6}$$

$$\frac{dM}{dt} = -5.2 \times 10^{-14}t^5 + 5.9 \times 10^{-11}t^4 - 2.4 \times 10^{-8}t^3 + 3.8 \times 10^{-6}t^2 - 5.9 \times 10^{-5}t - 2.4 \times 10^{-3} \tag{2.7}$$

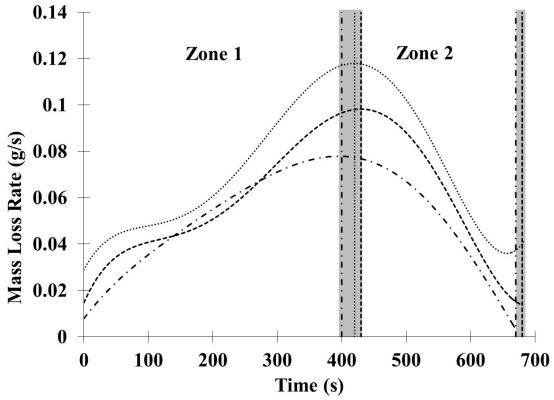

Figure 2.5: Equations 2.8, 2.9 and 2.10 are plotted to show the mass loss rate of the 4 cm channel width trials. The 4 cm channel width trials were less effected by the depth of fuel within the ice channel and resulted in a higher rate of mass loss over the entire duration of the trial.

$$\frac{dM}{dt} = 6.1 \times 10^{-15}t^5 - 1.0 \times 10^{-11}t^4 + 5.4 \times 10^{-9}t^3 - 1.4 \times 10^{-6}t^2 + 3.7 \times 10^{-4}t + 7.9 \times 10^{-3} \tag{2.8}$$

$$\frac{dM}{dt} = 2.9 \times 10^{-14}t^5 - 4.8 \times 10^{-11}t^4 + 2.7 \times 10^{-8}t^3 - 5.9 \times 10^{-6}t^2 + 6.3 \times 10^{-4}t + 1.5 \times 10^{-3} \tag{2.9}$$

$$\frac{dM}{dt} = 3.7 \times 10^{-14}t^5 - 5.8 \times 10^{-11}t^4 + 3.0 \times 10^{-8}t^3 - 5.7 \times 10^{-6}t^2 + 5.2 \times 10^{-4}t + 2.8 \times 10^{-2} \tag{2.10}$$

2.2.2 Dimensionless Analysis

A notable anomaly within the data set of the 2 cm mass loss rate (Fig. 2.4) is the doubling of the rate. The increased rate is attributed to the formation of the channel which resulted in approximately twice the amount of fuel being added to maintain a 4 cm channel width. It must be remembered that each channel

was individually created make variations in the exact dimensions quiet possible. In an attempt to correct for the influence of starting mass a dimensionless form of mass loss ($(massofconsumedfuel/initialmass)$)was used for comparison. The dimensionless unit of mass equates to what can easily be construed as an efficiency if it is multiplied by 100. Figure 2.6 provides a 6th order polynomial trendline of the dimensionless form of mass loss. It is easy to see that the significance of the increased fuel load on the 2 cm channel is not nearly as severe as it appeared to be in the dimensional form. Also what is noticeable is that the entire range of dimensionless mass loss is within a narrow range of 8% - 14% efficient.

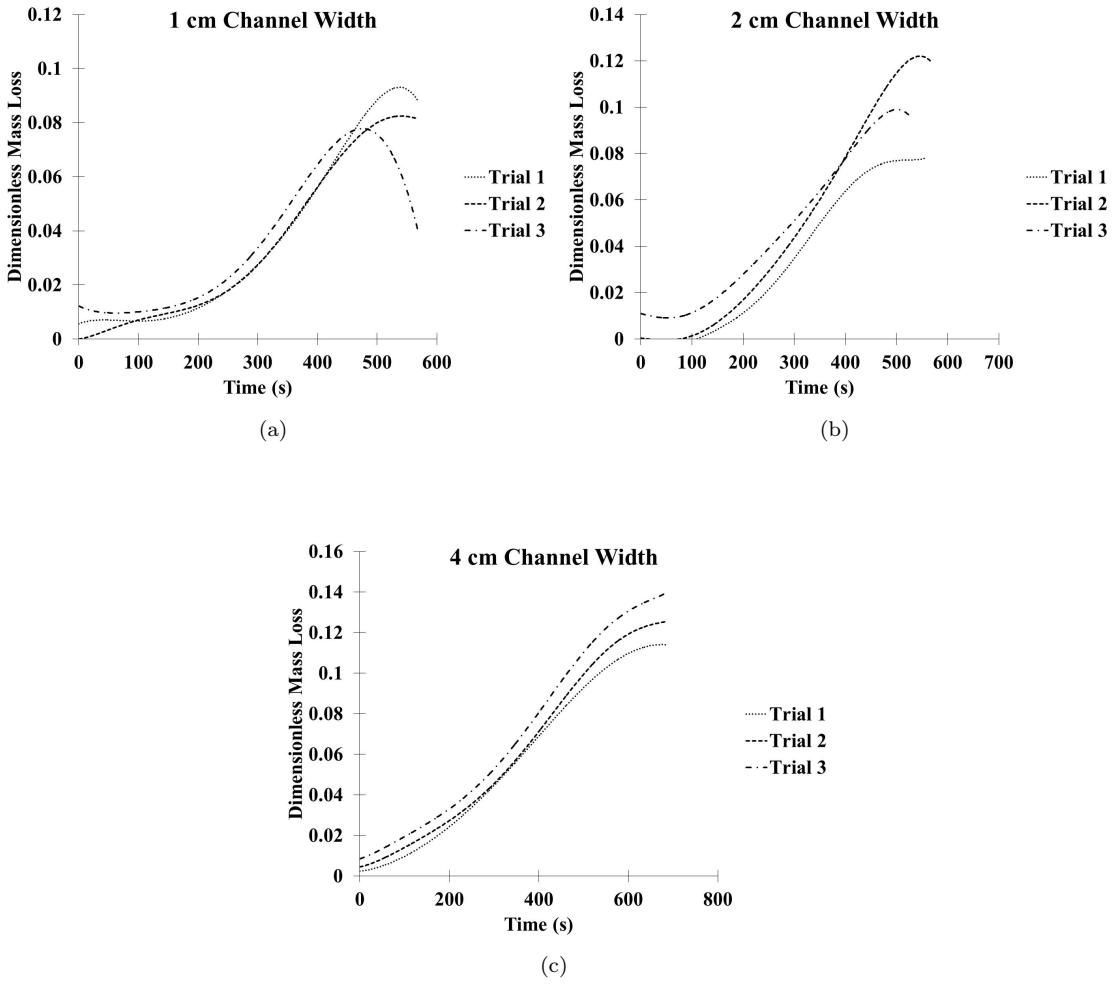

Figure 2.6: The plot of efficiency provides a means of comparing the performance of the various trials without the influence of initial fuel mass

For a more complete comparison to the data presented in §2.2.1 the derivative of the above trend lines were obtained.

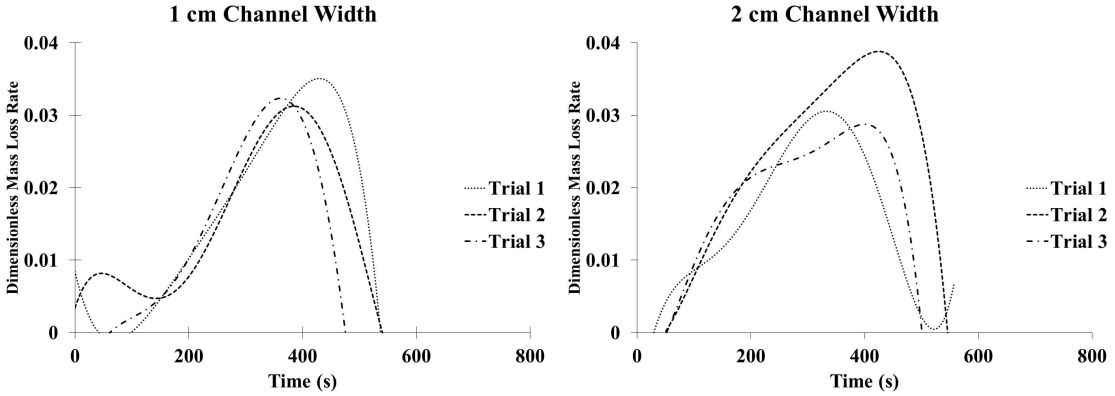

(a)

(b)

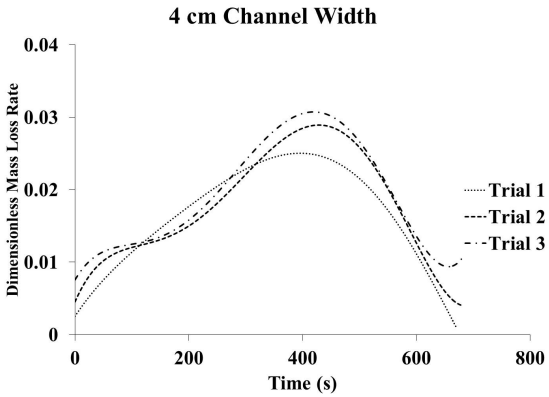

(c)

Figure 2.7: The plot of efficiency provides a means of comparing the performance of the various trials without the influence of initial fuel mass

2.2.3 Ice Channel Dynamics

Once the fuel layer reached height between 7 cm - 9 cm it no longer rose vertically but rather pushed laterally; thereby creating a lip in the channel wall (Fig. 2.10). Similar behavior is also observed during lava flow. The fissure formed (due to lava melting the ground) creates erosion channels similar to the lip formed in the current experiments [24].

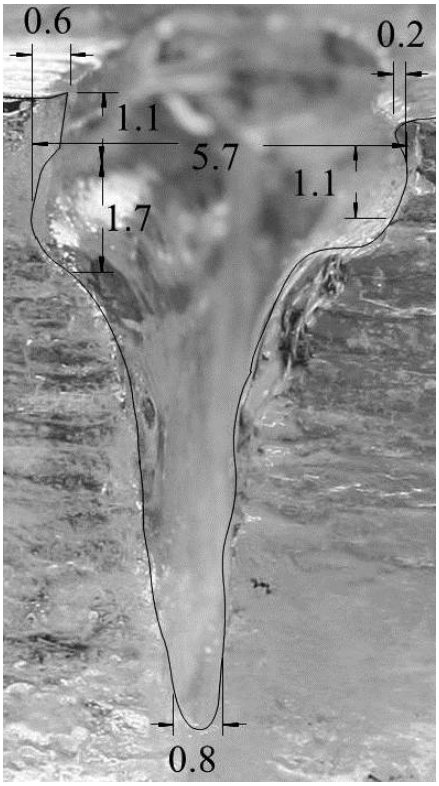

Figure 2.8: The final channel profile for a 1 cm channel trial is outlined in black and the dimensions of the ice lip are overlaid. The fuel layer only minimally penetrated the channel wall before the multifaceted cooling effects, compounded with the thinning fuel layer, led to flame extinguishment.

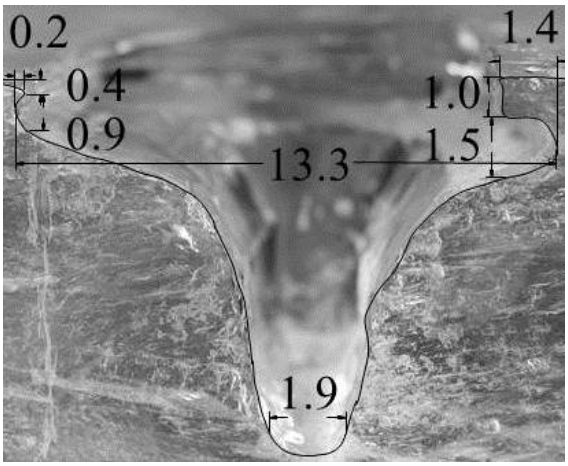

Figure 2.9: The final channel profile for a 2 cm channel trial is outlined in black and the dimensions of the ice lip are overlaid. Channel wall penetration was greater than the 1 cm channel width trials and is an indication of a higher fuel layer temperature due to a less restricted burning environment. The causes of the influences to the fuel layer temperature are discussed in further detail in §2.2.4.

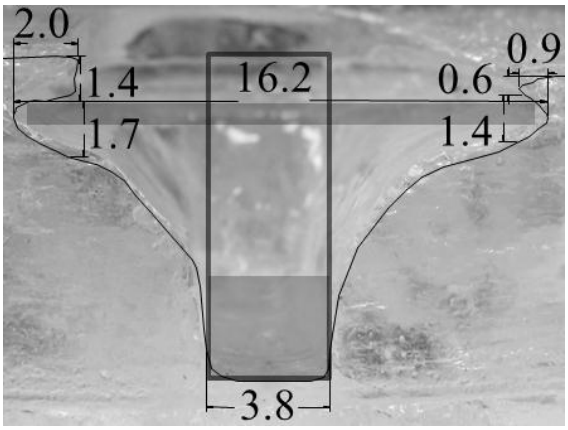

Figure 2.10: The final channel profile for a 4 cm channel trial is outlined in black and the black box indicates the original channel shape. The gray box on the bottom of the channel indicates the original fuel depth and the gray box at the top of the ice block indicates the final fuel depth.

Conduction losses from the sides are amplified by the multifaceted conductive face of the cavity formed in the ice channel wall. The resultant effect is a rapid deceleration of the mass loss as the fuel layer thickness falls below its critical thickness for sustained combustion. This region (decay from the peak mass loss rate to extinction) is defined as zone 2 in Fig. 2.3, 2.4 and 2.5. In addition to the increase in conduction losses, the brevity of zone 2's duration may also have been due to the multicomponent fuel mixture which required increasingly higher temperatures to sustain ignition as the lighter end volatiles were consumed. The dynamic effects of the channel width and the effect on mass loss rate are further discussed in §2.2.3 and §2.2.4.

The 1 cm trial and 2 cm trials required multiple ignition attempts which is noted on Fig. 2.3 and Fig. 2.4 by the area of the graph between $t = 0$ and the start of the mass loss rate curves. The gray areas on Fig. 2.3, 2.4 and 2.5 are intended to highlight the transition periods between pre-ignition and zone 1 (Fig. 2.3 and Fig. 2.4 only), zone 1 and zone 2, and zone 2 to extinction.

The increase in the mass loss rate during zone 1 is mainly due to the increased effective diameter of the oil slick due to the melting of ice and widening of the channel as shown in Fig. 2.8, 2.9 and 2.10. The melting of ice is an endothermic process and a significant portion of the heat evolved due to the combustion of fuel is lost in converting the ice into water. However, the melted water flows down below the channel thereby increasing the level of oil with respect to the surface (decreases the ullage height). Secondly as the ice melts, the channel widens thereby increasing the effective diameter of the oil spill. These two effects (decrease in ullage height and widening of the burning area) tend to overpower the heat loss effect due to heat conduction and heat loss due to ice melting and cause the mass burning rate to increase with time as observed in Fig. 2.3, 2.4 and 2.5 [25].

The average ending fuel layer thickness of the 1 cm 2 cm and 4 cm primary trials were 0.4 cm, 0.6 cm and

0.8 cm, respectively. The critical thickness to support ignition in an icy environment ranged from 0.3 cm to 1 cm depending on the fuel. For fresh crude oils, a critical thickness of 0.3 to 0.5 is expected [10]. A primary difference in the critical thickness reported in the published data compared to the data collected from these experiments are the dynamic effects of the ice channel. The melting ice channel allows the fuel layer to widen. The majority of the previous research involved large rigid containers containing a fixed percentage of ice cover. Once the ice melted away the fuel layer remains fixed [1–4, 6–10].

The burning behavior within an ice channel is illustrated in the schematic shown by Fig. 2.11. Figure 2.11 shows the dynamic nature of the burning behavior of oil mainly due to the melting of ice in the channel which causes the shape of the channel to change with time and the corresponding mass loss rate. The resulting influence on the mass loss rate of fuel is analyzed for the first time in this study and is the most unique aspect of the current series of experiments. As shown in Fig. 2.11b, the slick begins as a deep ullage pool fire and the mass burning rate is predominantly a function of the width of the channel; the wider the width the greater the initial mass burning rate as shown in Fig. 2.11c. Figure 2.11c shows the widening of the channel due to melting of ice. At the same time, the melted water flows down into the channel thereby raising the oil layer closer to the surface. This results in a decrease in the ullage height (height of the oil layer from the surface) as well as an increase in the surface area causing the initial 3 cm thick oil layer to thin out as it moves closer to the surface. Eventually, the thin oil layer which is close to the boiling point of the oil (236 ^{o}C, Tab. 2.1) melts the ice to form an "ice lip" as shown in Fig. 2.11d.

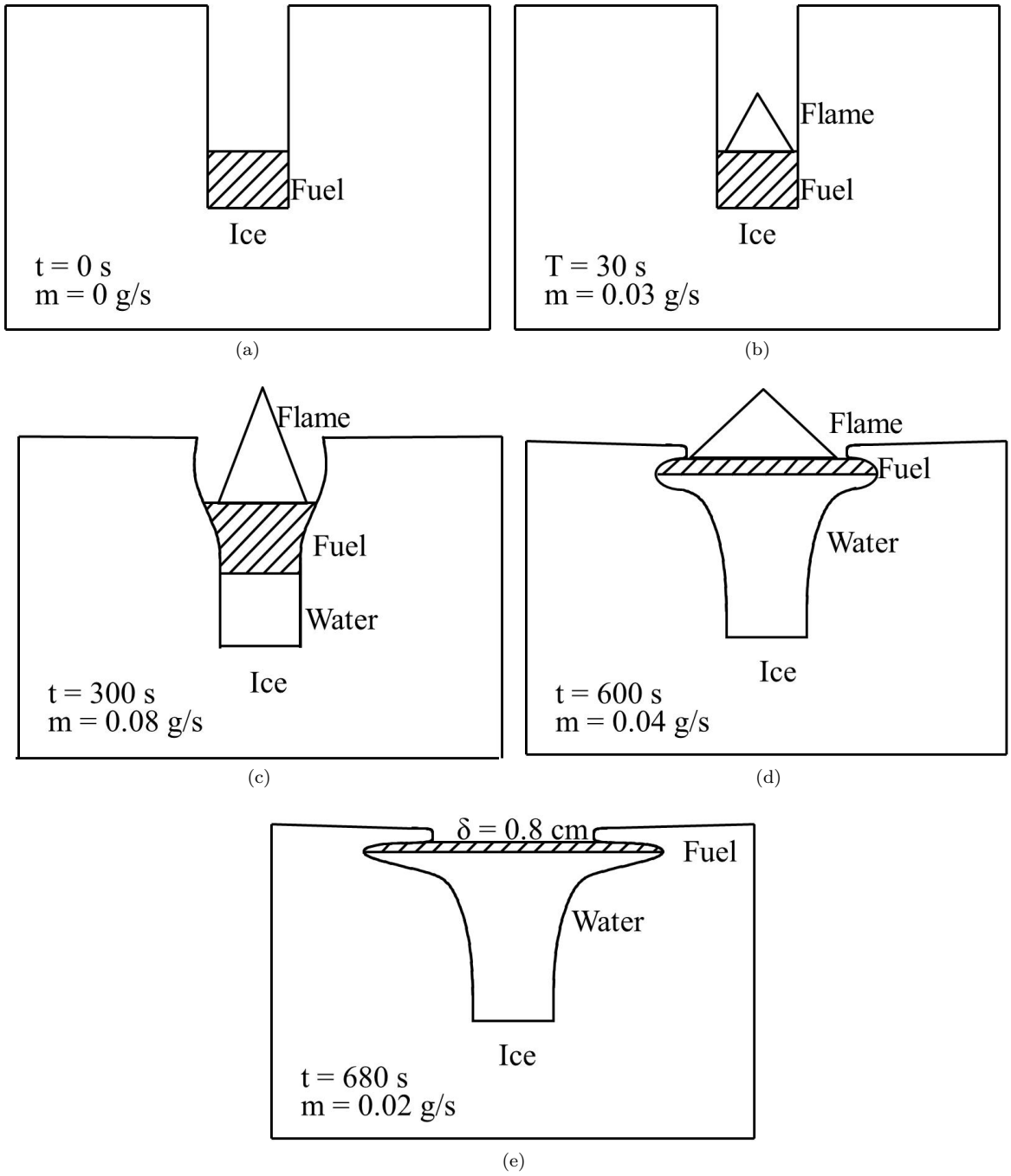

Figure 2.11: Profile of the ice channel over the course of a typical primary ice channel trial. The schematic has been modeled after a 4 cm channel width, however, the same stages occur in the 1 cm and 2 cm channel width, only to lesser degrees.

The unique formation of the ice lip was prevalent in all trials and certain patterns were noted. The average value of dimension x in Fig. 2.12, which is the distance from the top of the fuel layer to the top of the ice block (referred to as ice lip) at the end of each trial, was between 0.4 to 1.1 cm (the difference resulted

from flame tilting which resulted in preferential melting in some trials). The average value of dimension y in Fig. 2.12, which is the height of the ice cavity formed by the penetrating fuel layer was consistently; 1.6 cm on the left side and 1.5 cm on the right side (this dimension was not affected by flame tilt). Since the rise of the fuel layer was a result of melted water, the volume of melted water, is proportional to the channel width. The average, value of dimension z in Fig. 2.12, which is the penetration depth of the fuel layer into the ice channel, was not consistent between channel widths and is what determines the prominence of the ice lip. When the channel was 1 cm wide, an average penetration of 0.6 cm was observed and a final channel profile very similar to Fig. 2.11c was observed. The 4 cm channel had an average penetration of 1.8 cm, resulting in a channel profile similar to Fig. 2.11e.

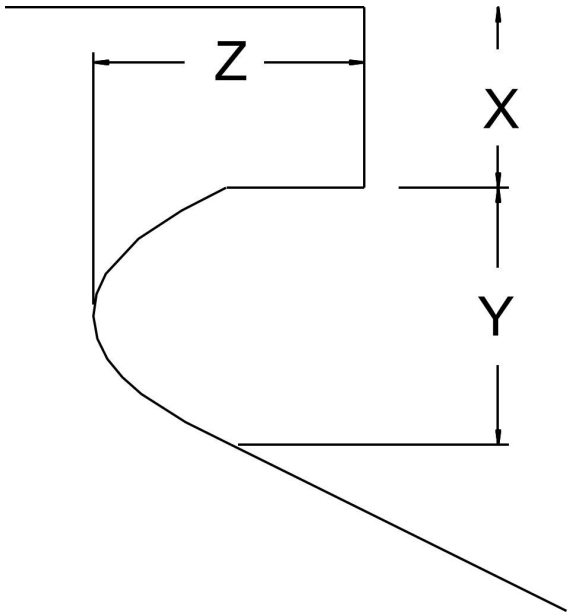

Figure 2.12: The relevant ice cavity dimensions where x is the distance from the top of the fuel layer to the top of the ice block; y is the height of the ice cavity formed by the penetrating fuel layer; and z is the penetration depth of the fuel layer into the ice block.

2.2.4 Temperature Profile

The temperature along the centerline of the ice channel was measured to provide insight into the effects taking place within the fuel layers over the course of each trial. Figure 2.13 provide a 10 second moving average plot of the temperature within the ice channel for the third trial of each channel width. A 10 sec moving average helps to smooth out the highly transient temperature measurements. The remaining portions of the data set can be found in Appendix A.

As described in §2.1, the seven thermocouples are spaced at 2 cm intervals, starting from the bottom of the ice channel. Each thermocouple temperature profile is represented by a gray line. The 2 cm thermocouple

was constantly in contact with cold liquid and is not shown. The low temperature does not provide much insight into the dynamics of the fuel layer other than confirming that the water layer remained near the freezing point of water.

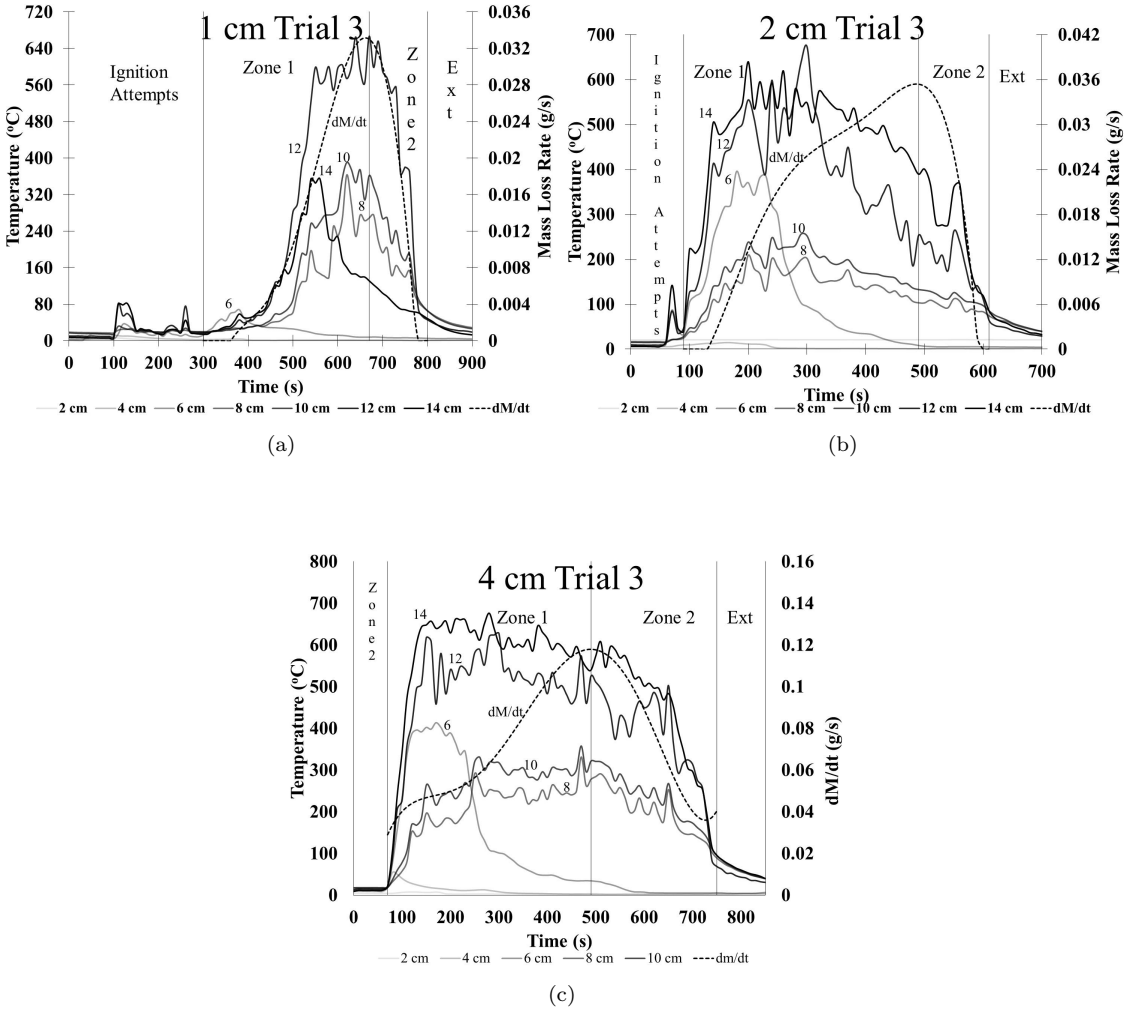

Figure 2.13: The 1 cm temperature profile provides insight into why the mass loss rates were s low which is evident by the brief period of intense heating. The 2 cm temperature profile is more in line with what would be expected from a typical pool temperature profile. The 4 cm temperature profile has a brief period of sustained, intense heat release during the initial 100 seconds of burning.

For demonstration purposes the mass loss rate (dM/dt line) of each trial was plotted on the secondary y-axis. Having the mass loss rate on the same figure as the temperature profiles facilitated the analysis of the channel dynamics. Figure 2.13a and Fig. 2.13b have a period of time prior to the start of zone 1 where multiple ignition attempts were necessary before a self-sustaining flame was present. During the ignition period temperature readings are present but are not considered influence the measured mass loss rate the mass loss rate, given the accuracy of the load cell being ± 0.5 grams. Due to the assumption that

the ignition time does not influence the measured mass loss rate, the dM/dt line begins at a point where there is appreciable temperature augmentation across the thermocouples. The zone lines, similar manner as Fig. 2.3, Fig. 2.4 and Fig. 2.5, are also shown to see how the temperature changes over the different stages.

The amount of fuel used in each trial was based on the position of the 4 cm thermocouple. During the setup of each trial the fuel was poured into the ice channel until it met the 4 cm thermocouple. This ensured that the fuel layer surface temperature was measured during the beginning of every trial. The temperature plot at the 4 cm thermocouple briefly increases before the melted water moves the fuel surface above the 4 cm thermocouple which results in the thermocouple measuring cold oil and melted water.

Figure 2.14 provides a depth versus temperature plot. The temperature profile of the liquid within each ice channel, at various points in time, facilitated the analysis of the upward progression of the fuel layer. In each trial there was an early increase in the 6 cm thermocouple temperature followed by a sudden decrease. The early temperature increase was attributed to the low initial flame height (Fig. 2.11b) while the rapid decrease was attributed to the melted water pushing the fuel layer above the thermocouple (Fig. 2.11c). In the early stages of the trial the highly volatile petroleum ether was driving the combustion process, generating a sufficient quantity of heat to melt the channel walls and progress the trials into the later stages. As discussed in §2.2.5 the petroleum ether burned rigorously in ice channel and it should be assumed that if it was not for the petroleum ether acting as a accelerant the *in situ* burn would fail. This assumption can be made due to the fact that the motor oil alone has an appreciably high flash point and that it would be difficult to ignite even outside of an ice channel.

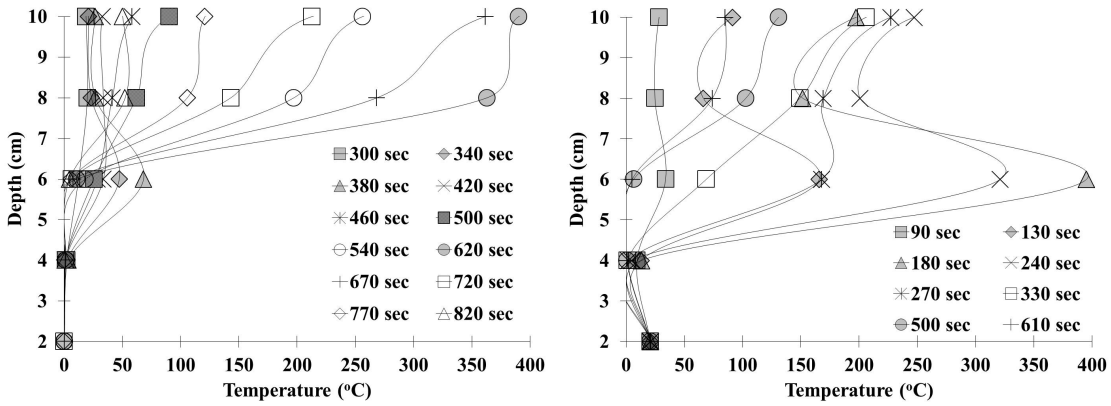

(a) (b)

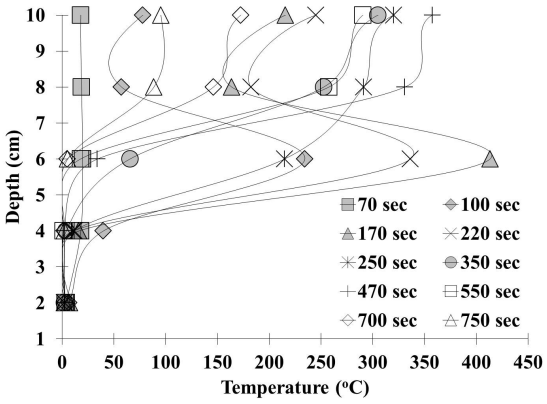

(c)

Figure 2.14: The temperature profile through the depth of the ice channel width provides insight into the rate of the fuel layer as the channel walls melt. The fuel layer quickly rises to beyond the 4 cm and 6 cm thermocouple and then stagnates between the 8 cm and 10 cm thermocouple as the fuel layer spreads horizontally.

At a point between the 6 cm and 8 cm thermocouple the fuel layer no longer moves in the vertical direction but begins to move horizontally, penetrating the walls of the ice channel. This movement corresponds to a stagnation of the temperature profile, observable at the 8 cm and 10 cm thermocouples. These thermocouples reach a maximum temperature then systematically decline in unison until extinction; indicating a lack of vertical motion. The maximum temperature corresponds to the maximum mass loss rate and the formation of the ice lip. From the transition point the temperature of the liquid phase steadily declines as the critical thickness of the fuel layer is exceeded. The consistent behavior of temperature profile between the nine trials provides evidence to suggest that the point at which ice wall penetration occurs is independent of channel width.

Since the fuel layer is comprised of a multi component fuel the temperature necessary to sustain combustion will increase over time. As previously mention in §2.2.1, the decreasing fuel layer thickness and penetration into the ice increase the conductive losses and prevents the fuel layer from achieving the necessary temperatures to volatize the heavier components on the motor oil. At the maximum temperature, there is a steep temperature gradient between the 8 cm and 10 cm thermocouple. The steep temperature gradient provides evidence to suggest that the losses into the water layer are significant. Another indication of significant quantities of heat passing through the fuel layer and into the water layer was the presence of bubbles in/under the fuel layer. These bubbles are presumed to be water vapor resulting from heating of the water sublayer. Given a longer duration burn, boiling of the water sublayer would occur and result in an increase in the mass loss rate. [26] It should be noted that the bubbles seen in Fig. 2.15 were only noticed in the 4 cm trials. As the trials progress through zone 2 the deceasing fuel layer thickness, increasing

conductive losses and changing fuel composition act to extinguish the flame.

Figure 2.15: Bubbles are present in the lower left corner of the final 4 cm channel width pool. Bubbles were only observed in the 4 cm channel width trials.

The high temperatures early in the 2 cm trial lead to the ice channel walls early melting of the channel walls and to the critical thickness being met sooner than in the 1 cm trial. This is why the 1 cm trials and 2 cm trials have comparable trial durations despite the 2 cm trial have more fuel and more availability to oxygen.The increased heat produced during the 4 cm trial is attributed to the larger mass of fuel, which has more light ends, and larger initial channel width, which encourages the combustion process.

2.2.5 Auxiliary Trials

To better understand the results of the primary trials two additional trials were conducted to aid in defining the bounds of the problem. The Fig. 2.16 represents a case where 58 grams (approximately 2.5 cm layer) of petroleum ether was ignited in a 1 cm wide channel.

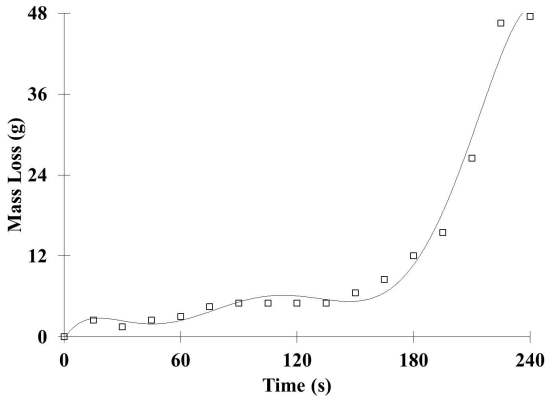

Figure 2.16: The mass loss rate of the petroleum ether is presented in the figure. The boxes represent each data point taken at 15 second intervals and span the ±0.5 gram accuracy of the load cell.The 6th order polynomial fitted over the data is seen in Eq:2.11.

$$\begin{aligned} dM = &-2.2 \times 10^{-11} t^6 + 1.5 \times 10^{-8} t^5 - 3.7 \times 10^{-6} t^4 \\ &+ 4.1 \times 10^{-4} t^3 - 2.1 \times 10^{-2} t^2 + 4.3 \times 10^{-1} t - 2.5 \times 10^{-1} \\ r^2 = &\ 0.98 \end{aligned} \tag{2.11}$$

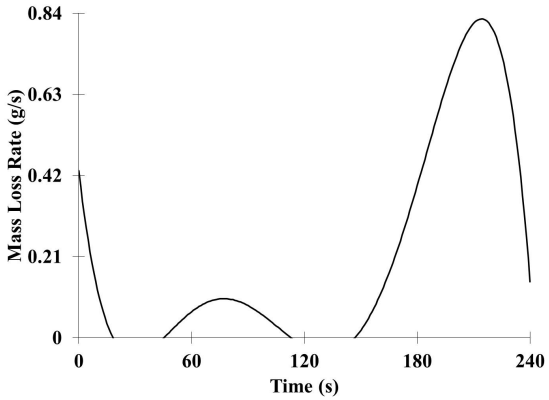

Figure 2.17: The negative values in the mass loss rate do not represent negative mass loss (gaining of mass) but miscellaneous construct of the methods used to determine mass loss rate and should be interpreted as no mass change in mass loss rate. The equation for the mass loss rate of petroleum ether in a 1 cm ice channel is given in Eq:2.12.

$$\begin{aligned} dM = &-1.3 \times 10^{-10} t^5 + 7. \times 10^{-8} t^4 - 1.5 \times 10^{-5} t^3 \\ &+ 1.2 \times 10^{-3} t^2 - 4.2 \times 10^{-2} t + 4.3 \times 10^{-1} \end{aligned} \tag{2.12}$$

The petroleum ether trial starts out at a high mass loss rate but then rapidly decays indicating that the small channel width causes oxygen starvation. The melted water eventually decreased the ullage of the fuel layer until the fire once again starts to burn vigorously. The petroleum ether trial had to be stopped prematurely due to the overflow of the fuel layer into the plastic tray. The results of the petroleum ether trial prove that light-end hydrocarbons are not appreciably hindered by the conductive losses and instead the early stages of the problem are governed by the ullage height. The period of melting is represented on Fig. 2.17 by the period of time in which the mass loss rate is oscillating between negative and positive mass loss rates.

The second auxiliary trial comprised of the 4 cm channel covered with a thin metal foil to ensure that the fuel layer was not interacting with the melted water. The results of the foil trial yield a constant mass loss rate which which starts at a maximum rate and burns for approximately three times as long as the corresponding run in a 4 cm ice channel. Comparing the two curves (with and without metal foil) the maximum mass loss rate for the case without the foil approaches the steady-state mass loss rate of the foil, surpasses it and then quickly reaches extinction. The decay in mass loss rate of the foil trial can be attributed to two mechanisms, both of which are a direct result of the consumption of fuel. The first mechanism is a deepening of the ullage height and the second is the preferential volatization of the lighter end compounds. On the other hand, the increase in the mass loss rate without the foil trial is initially due to the decrease in ullage height due to the melted water raising the oil in the vertical direction and later-on due to widening of the channel walls, thereby increasing the surface area exposed to the ambient.

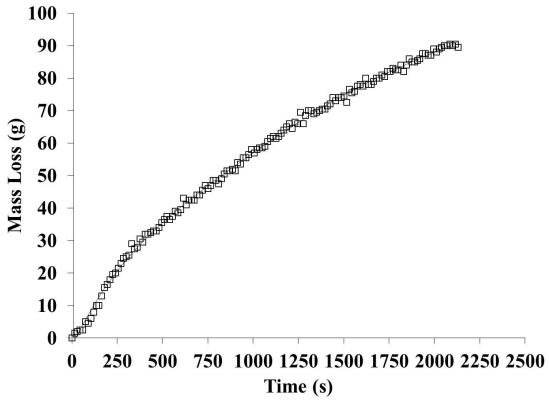

Figure 2.18: The mass loss within the metal channel is appreciably greater than the even the strongest ice channel trial.The 6th order polynomial fitted over the data is seen in Eq:2.13.

$$
\begin{aligned}
dM = &-5.4 \times 10^{-19} t^6 + 1.0 \times 10^{-14} t^5 - 5.1 \times 10^{-11} t^4 \\
&+ 1.1 \times 10^{-7} t^3 - 1.3 \times 10^{-4} t^2 + 1.2 \times 10^{-1} t - 2.8 \\
r^2 = &\ 0.99
\end{aligned}
\tag{2.13}
$$

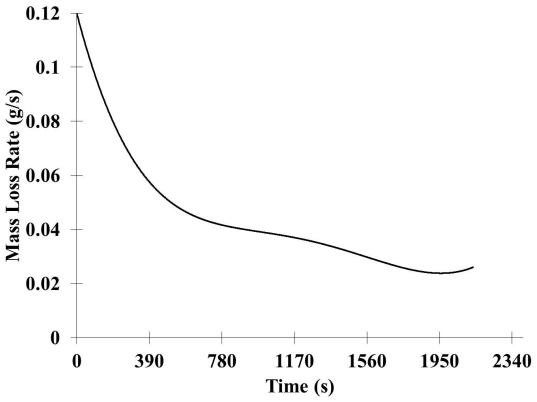

Figure 2.19: The mass loss rate in a metal lined channel starts out a a maximum but over the course of the trial approaches a rate comparable to the primary trials. The equation of the mass loss rate in a metal channel is given by Eq:2.14.

$$
\begin{aligned}
dM = &-3.2 \times 10^{-18} t^5 + 5.1 \times 10^{-14} t^4 - 2.1 \times 10^{-10} t^3 \\
&+ 3.4 \times 10^{-7} t^2 - 2.7 \times 10^{-4} t + 1.2 \times 10^{-1}
\end{aligned}
\tag{2.14}
$$

For better comparison of the effect of channel width on the mass loss rate an average mass loss rate for each channel width was taken and charted using a logarithmic scale (Fig. 2.20). The 4 cm channel width trials plot has a unique shape, compared to the 1 cm and 2 cm channel widths, and is indicative of a steady mass loss rate over the duration of the trial. However, as previously described, a common behavior exists between the three channel widths: starting at a minimum mass loss rate, increasing to a maximum mass loss rate and rapid decay to extinction.

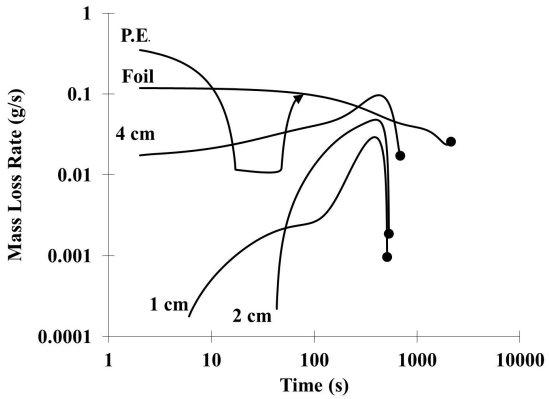

Figure 2.20: A comparison of the three primary trials to the two alternative trials highlights the difficulty of achieving high mass loss rates in a dynamic ice environment with a fuel that has a relatively high flash point. The solid circles at the end of primary trials and foil trial indicate that the flames self-extinguished; the arrow at the end of the petroleum ether trial indicates that the flame was manually extinguished.

Table 2.2 provides the maximum mass loss rate of each trial and the time at which it occurs, based on Fig. 2.20. The petroleum ether trial was 83% efficient, the foil trial was 37% efficient, the 4 cm trial was 12% efficient, the 2 cm trial was 10% efficient and the 1 cm trial was 10% efficient. Though the conductive losses to the ice are significant enough to prevent the total consumption of the fuel mixture in the foil trial, the observations made from the two auxiliary trials show that for the heavier compounds it is the dynamic effects of the ice which govern the mass loss rate and not the cooling effects of the ice.

Table 2.2: Peak Mass Loss Rate

	MLR (g/s)	Time (s)
1 cm	0.03	380
2 cm	0.05	390
4 cm	0.1	420
Foil	0.12	0
P.E.	0.43	0

2.3 Conclusion

A series of experiments were conducted to develop an understanding of *in situ* burning of an oil spill within an ice channel. The mass loss rate of a fuel layer within an ice channels of varying widths was studied to understand how channel width affected mass loss rates. The mass loss rate is primarily limited by ullage and fuel layer depth and less affected by channel width. Melting of the ice channel over the course of the trial created a highly dynamic burning environment. Decreased ullage and increased fuel surface area over the course of each trial normally serve to increase mass loss rates. Due to heat losses and a rapid decrease

in the fuel layer depth any benefits are quickly overcome. The rapid decrease in fuel layer depth is the more prominent factor is reducing mass loss rates. The temperature profiles along the centerline of the oil layer were used to physically explain the reason for the formation of an ice-lip which was formed towards the end of the burning-phase. This unique behavior definitely warrants future study.

Chapter 3

Spreading

Introduction

Obtaining the spread rate of a spill provides oil spill coordinators the necessary information to plan an effective response effort. When the spread rate is correctly estimated it can aid in the decision to use conventional clean up methods or identify the need to look for alternatives. A critical parameter of *in situ* burning is the thickness of the slick. On average, it is recognized that a minimum slick thickness of 1 mm is needed to sustain a burn on cold water for fresh crude oil [9]. Due to the surface roughness of ice the slick will be nonuniform. Additionally, the cold temperatures will reduce they slick's ability to spread by reducing the viscosity of the oil. The reduction in spread rate that the ice may impart would assist in an *in situ* burn by maintaining the depth of the slick above the critical thickness for a greater length of time.

Experiments are performed using ice channels of varying widths. A condition of rapid discharge of oil is used to replicate a punctured vessel leaking onto an ice sheet. To our best knowledge, no model exists which can exactly replicate the described scenario; therefore two more general models that consider buoyancy-driven spreading over a horizontal surface are chosen to compare against the experimental data. The first is an inviscid model wherein a constant front speed is assumed [27]. The second is a viscous model; it presumes that the current is sufficiently thin so that buoyancy forces balance viscous forces and the front speed is a decreasing function of time. [27].

3.1 Methodology

The spread rate of oil on solid ice was studied by releasing an oil mixture along a 96 cm long, 4 cm deep rectangular channel cut into a block of ice as shown in Fig. 3.1. The width of the channel was varied as 1

cm, 2 cm and 4cm. Each channel was individually created using a saw to removed the bulk material. Then a chisel was used to smooth the edges and create uniformity along the channel length. The source of the oil mixture was a 500 ml burette, with a 1 cm wide (outer diameter) orifice, placed at the center of the channel. The amount of oil used for each trial was based on the amount of oil needed to fill the ice-blocks used to study the burning behavior to a depth of 4 cm (Fig. 3.1). Thus the 1 cm trials used 100 ml of the oil mixture, the 2 cm trials used 175 ml of the oil mixture and the 4 cm trials used 300 ml of the oil mixture. The overarching intent of these multifaceted experiments was to draw conclusions between the spread rate and mass burning rate of an oil slick by keeping the oil thickness constant for all widths tested. The mass loss rate study can be found in the Proceedings of Combustion Institute's 34^{th} International Symposium on Combustion.

A video camera was used to record the movement of the leading edge of oil as a function of time. Seven thermocouples (K-type, wire diameter 0.125 cm) spaced at 12 cm intervals were also used to track the spread rate of the oil. A noticeable temperature spike was observed when the leading edge of the oil first touched a thermocouple. This was used a time-marker and compared with the video camera data as an additional check on the accuracy of the spread-rate.

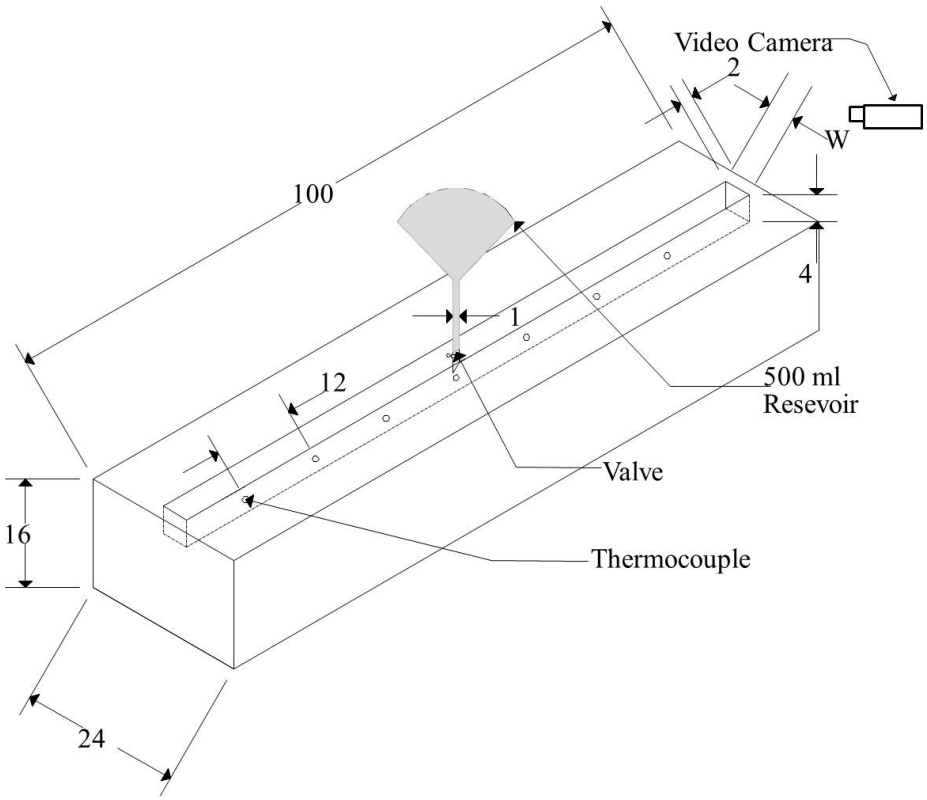

Figure 3.1: experimental setup to study the spread of oil in an ice channel. W = 1, 2 and 4 cm. The average flow rate of the burette, based on total time to expel the contents, was 5.6 ml/s, 6.5 ml/s and 7.3 ml/s for the 1 cm, 2 cm and 4 cm channel widths, respectively. All dimensions are in cm unless otherwise noted.

The fuel used in the experimental setup was a hydrocarbon solution intended to simulate crude oil by having a mixture of light end and heavy end compounds. The fuel mixture consisted of three parts Castrol SAE 30 motor oil [21] to one part petroleum ether [22]. Table 3.1 lists the relevant physical properties [21–23, 28], where Re is calculated $Re = \frac{\sqrt{g'h_0}h_0}{\nu}$ where g' is a reduced gravity constant, h_0 is the height of the flow and ν is the kinematic viscosity [29]. A detailed description of how Re was obtained is located in Appendix B. The temperature of the oil was at ambient temperature (20^{o}C) when it entered the channel.

Table 3.1: Properties of Oil Relevant to Spreading

Density	ρ	844 kg/m^3
Flash Point	T_{fp}	161 ^{o}C
Boiling Point	T_{bp}	236 ^{o}C
Volume	V	100, 175, 300 ml
Avg. Flow Rate	$\dot{q}$	6.5 ml/s
Avg. Reynolds	Re	2.8, 1.5, 1.8

3.2 Results and Discussion

3.2.1 Controlling Mechanisms

When oil is poured inside the ice channel, it spreads in the form of a thin continuous layer. The spread rate is categorized by three primary regimes: buoyancy-inertial, buoyancy-viscous and surface tension-viscous. During the very early stages of an oil spill, inertial forces are the primary resistive forces while buoyancy is the primary driving force. The inertial force is measured as:

$$I = \frac{bh^3}{12} \tag{3.1}$$

Where I is the inertial force, b is the cross-sectional width and h is the height. Equation 3.1 implies that h dominates the inertial force and therefore as the current thins the inertial forces quickly diminish [30]. The weak inertial forces give way to viscous effects, which become the dominant resistive force when the current becomes long and thin. As the current approaches a mono-layer, buoyancy is no longer the primary driving force and instead surface tension pulls the slick outward. [20]

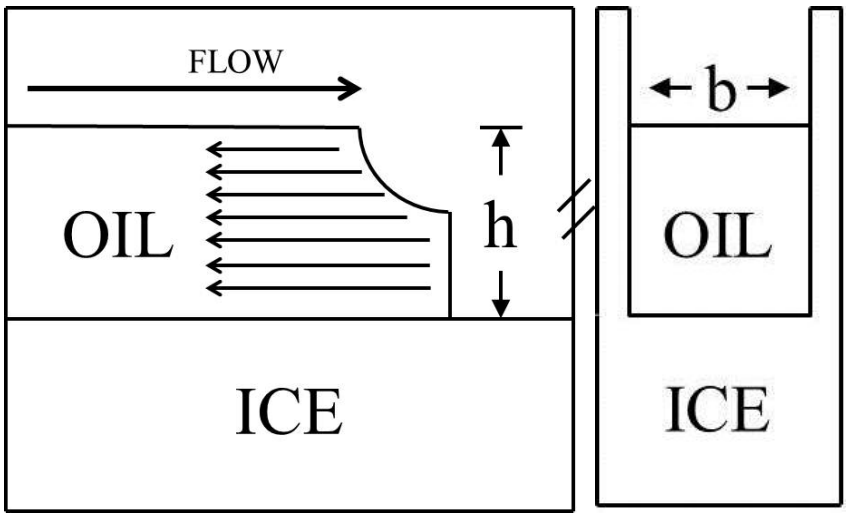

Figure 3.2: The main force retarding force (inertia) in the buoyancy-inertial spreading regime is represented by the arrows. The pertinent dimensions of Eq. 3.1 are depicted in both (a) and (b) where Fig. 3.2b is the cross-sectional view.

A current dominated by buoyancy and inertia and released over a brief interval of time from the burette described above will spread as a linear function of time. Conversely a flow dominated by viscosity will spread more slowly as we quantify below. The experimental apparatus did not allow for the current to spread far enough for surface tension effects to be appreciable. As a result of this, only the buoyancy-inertial and

buoyancy-viscosity regimes are considered. The surface tension-viscous regime may be irrelevant to field conditions in any event: the oil may become weathered beyond a point at which it would easily ignite [20].

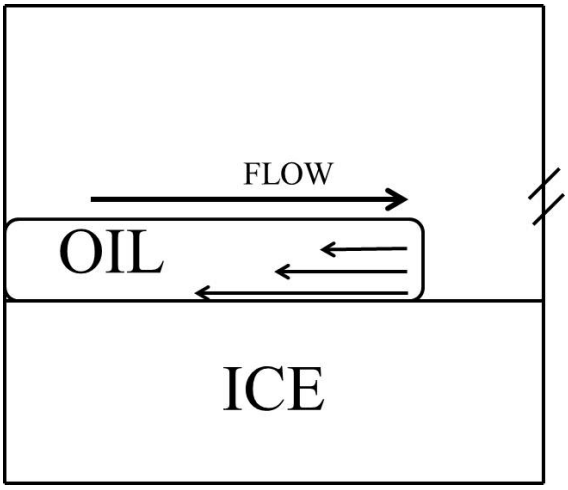

Figure 3.3: A thin slick in the forces in the buoyancy-viscous spread regime. The viscous forces are depicted by the arrows.

Fay [20] characterizes these three regimes using Eq. 3.2, Eq. 3.3 and Eq. 3.4, respectively.

$$D = \left(\Delta g V t^2\right)^{\frac{1}{4}} \tag{3.2}$$

$$D = \left(\frac{\Delta g V^2 t^{\frac{3}{2}}}{\nu^{\frac{1}{2}}}\right)^{\frac{1}{6}} \tag{3.3}$$

$$D = \left(\frac{\sigma^2 t^3}{\rho^2 \nu}\right)^{\frac{1}{4}} \tag{3.4}$$

Where D is the diameter of the pool, Δ is the density difference between the water and the oil, g is the gravity constant, V is the volume of the spill, t is the duration of the spill, ν is the kinematic viscosity of the oil, σ is the liquid surface tension and since these are order of magnitude calculations ρ is not distinguished between water or oil.

When analyzing a gravity current along a rigid surface it is important to recognize the role that non-slip condition imparts on the flow. Huppert [27] considered the flow of a high Reynolds number along a rigid two dimensional channel and as well as axisymmetric spreading. He noted that the flow of a fluid, as analyzed by Fay [20], will have a different distribution of forces given that the current is flowing over a free moving body.

3.2.2 Raw Data

Since the oil was released at the center of the ice channel two leading edges are formed, a left-hand side and a right-hand side. The configuration of the experiment allowed for two data sets to be collected per trial. Table 3.2, 3.3, 3.4 provides the time for the leading edge to progress along the channel. The average velocity for each trial was 0.07 cm/s, 0.07 cm/s and 0.03 cm/s for the 1 cm, 2 cm and 4 cm channel widths, respectively.

Table 3.2: 1 cm Spreading times along channels (s)

Length	Trial 1		Trial 2		Trial 3	
cm	RHS	LHS	RHS	LHS	RHS	LHS
12	2	2	1	2	2	2
24	5	5	2	3	4	4
36	7	8	6	5	6	8

Table 3.3: 2 cm Spreading times along channels (s)

Length	Trial 1		Trial 2	
cm	RHS	LHS	RHS	LHS
12	2	2	2	2
24	5	3	4	3
36	7	4	6	4

Table 3.4: 4 cm Spreading times along channels (s)

Length	Trial 1		Trial 2		Trial 3	
cm	RHS	LHS	RHS	LHS	RHS	LHS
12	4	3	6	2	6	3
24	11	4	13	4	12	7
36	17	11	19	9	18	14

3.2.3 Model Comparisons

One of the challenges of this investigation was to find a model that could predict the spread of oil inside an ice channel. That is, we are unaware of any model that predicts the front position of a spill of heavy liquid corresponding to the experimental conditions described above. To overcome the absence of a precise prediction tool, a pair of related models were instead applied to assess their accuracy in describing the flow dynamics of interest here.

The inertia dominated, or inviscid, model chosen for comparison with the experimental data is one which Ungarish [29] describes as:

$$x_n(t) = 2\left[1 - \sqrt{2\left(\frac{\rho_a}{\rho_c}\right)}\right] Ut \tag{3.5}$$

$$U = \sqrt{g' h_0} \tag{3.6}$$

$$g' = \frac{\rho_a - \rho_c}{\rho_c} g \tag{3.7}$$

Here x_n is the front position in m, ρ_a is the density of air in kg/m^3, ρ_c is the density of the oil in kg/m^3, U is the velocity scaling factor in m/s, t is the time s, h_0 is a characteristic current depth in m, g' and g are, respectively, the reduced and standard gravitational accelerations in m/s^2. Equation 3.5 predicts the frontal position of a heavy current ($\rho_a/\rho_c \ll 1$) intruding into a rigid two-dimensional channel which has been released en masse, i.e. from a lock release apparatus.

h_0 is assumed to be the height of current upon reaching the first thermocouple (12 cm) at the given flow rate of 5.5 ml/s, 6.5 ml/s and 7.5 ml/s and an average transit time of 1.8 s, 2.0 s, and 4.0 s.

$$h_0 = \frac{\dot{q}\bar{t}}{A} \tag{3.8}$$

Where $\dot{q}$ is the average flow rate, $\bar{t}$ is the average transit time to the first thermocouple and A is the cross-sectional area of the channel.

The viscous current chosen for comparison with the experimental data is one which Huppert [27] describes as:

$$x_n(t) = \eta_N \left(\frac{\frac{1}{3} g' q^3}{\nu}\right)^{\frac{1}{5}} t^{\frac{3\alpha+1}{5}} \tag{3.9}$$

Where x_n is again the front position in m, η_N is defined as the similarity value and taken as 1.411. q is the volume per unit width in cm^2, α is the mass flow growth factor given as 0 for this scenario and ν is the kinematic viscosity in m^2/s. Equation refeq:5 has an asymptotic front speed as $t \to 0$ resulting in an offset in the predicted frontal speed to the observed frontal.

Figure 3.4 shows that Eq. 3.9 is a more accurate predictor of the frontal position than Eq. 3.5 although neither equation seems to be especially applicable here. There are three possible reasons why the experimental data does not show better agreement with Eq. 3.9. Firstly, Eq. 3.9 is an asymptotic equation that is expected to apply after some initial transient. Conversely for early times, it predicts large front speeds, which are not observed in the laboratory. The fact that the dotted and solid lines of Figure 3.4 have similar profiles

(though are vertically offset from one another) supports this point of view. Second, Eq. 3.9 assumes a purely 2D flow in the absence of sidewalls, which are present in our experiments and which exert additional shear forces. Thirdly, and especially for the 4 cm channel, there is in our experiments an initial transient phase during which the oil spreads across the width of the channel; only thereafter is the primary flow along the channel length.

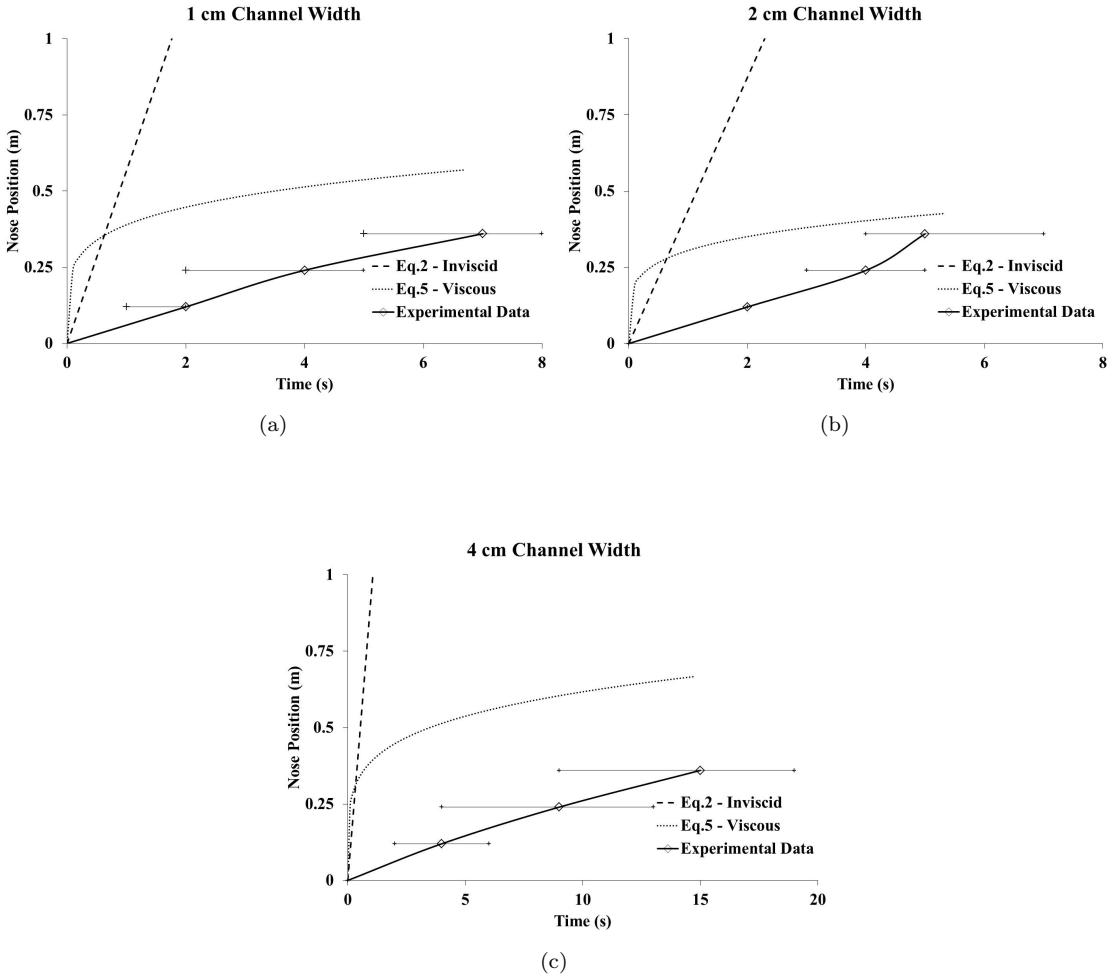

Figure 3.4: The experimental data is compared against a model which predicts the front position a gravity current with the buoyancy-inertial spreading regime (inviscid) and the buoyancy-viscosity spreading regime. Where (a) provides the data from the 1 cm channel width (b) provides the data from the 2 cm channel width and (c) provides the data from the 4 cm channel width. The inviscid current model is truncated after 3 seconds as it over predicts the experimental data. The light black lines show the range of data by spanning the high and low data.

3.3 Conclusion

A series of experiments were conducted to develop an understanding of the spreading of a current within an ice channel. The work provides a means of comparing spread rate within an ice channel to published theoretical models. Given the relatively low Reynolds of the flow, the viscous spreading model of Huppert [27] was found to be a more accurate prediction of the front position than the inertial spreading model described by Ungarish [29]. Future work is needed to evaluate how progression of an oil slick will respond to variations in flow rates. Based on the provided analysis the implication to oil spill response is the oil will not spread quickly and therefore make *in situ* burning a feasible option.

Chapter 4

Conclusions & Future Work

The purpose of this study was to provide an analysis of the behavior of oil in direct contact with ice for the purpose of *in situ* burning. An oil spill on ice poses a unique threat given that most locations of Arctic oil exploration and production are extremely remote and resource limited. Therefore, an *in situ* burn may be the most economical and effective option.

The bench-top testing for oil burning in an ice channel indicates that *in situ* burning of oil in ice is primarily limited by ullage and fuel layer depth. Given the tendency of the fire to consume the available oxygen and the cooling effects of the ice/water on the slick, very low efficiencies, approximately 10%, were achieved. The melting of the ice channel created a highly dymanic environment which ultimately reduced the overall efficiencies by increasing the surface area. The ice channel deformation resulted in a reduction in the fuel layer depth to below a critical thickness ($\approx$1 cm). The efficiencies of the burn may increase as pool size increases and/or channel depth varies. Additionally, providing a constant external heat flux would assist the flame in achieving higher liquid temperatures and, consequently, higher efficiencies.

For oil spreading along an ice channel the current is more accurately represented by a buoyancy-inertia current lock-release model than a gravity-inertia lock-release model. The challenge of the experimental setup was that a model describing a variable flux into a 2D rectilinear channel has not been developed for comparison. The buoyancy-viscous lock-release model described by Huppert [27] over-predicts the frontal position of the current due to an initial asymptotic front speed at $t \to 0$ which is not observed in the experimental data. The experimental data does not exhibit a period of buoyancy-inertial dominated spreading and as a result the distances of the frontal position reported by Huppert's model [27] are offset by a given amount.

For the purposes of an oil spill response, *in situ* burning within an ice channel, based on the current body of research may not be as successful as past studies have reported. It would be suggested that for small

channel widths ($\leq$4 cm) oil may be ignited to bring the spilled oil to the surface where it could be collected by other means. One potential issue that may arise with burning of oil in an ice channel is the possibility that the penetrated oil may become trapped if the ice sheet were to refreeze. The potential for entraining oil in an ice sheet will need further validation.

Future work is required on both the mass loss chapter and the spreading chapter. For the mass loss rate further work is required to evaluate the ice lip formation. That is, what are the governing parameters involved with the formation and how may it affect the process of *in situ* burning. If further bench-scale tests are to be conducted, a more systematic approach using a simpler geometry is advised. The simpler geometry, such as a cylinder, would allow for an easier evaluation of the penetration and shape of the lip formation. Meso-scale, minimum of 1 meter in diameter, are recommended to determine if ice lip formations still occur at larger heat release rates. In larger scale tests, other factors such as relative flame height, smoke obscuration and channel length may become significant. Also, boiling of the water sublayer would be expected to occur as the water at the oil/water interface is heated to its boiling temperature. The boiling action would act to atomize droplets of oil above the fuel surface, creating a larger surface area to volume ratio fuel, and stir fresh fuel to the surface. Both of these events would lead to increases in the mass loss rate.

Future work on spreading along an ice channel should be focused on evaluating the frontal position of the slick in a 2D channel while varying the flow rate into the channel. It is expected that larger flow rate will have a more significant buoyancy-inertial flow rate in the early stages of the trial before transitioning to a bouncy-viscous flow. The effects of lateral spreading should to be evaluated within the contexts of the 2D channel since very wide channels, those approaching a square, will have axisymmetric spreading tendencies until the current comes in contact with the channel walls. Another point of interest would be to further evaluate varied Reynolds numbers by either changing the viscosity of the fluid or physical dimensions of the channel.

The research presented here has attempted to described the behavior of an ice channel for the purposes of furthering the body of knowledge pertaining to *in situ* burning of oil on ice and lay the foundation for future work relating to direct oil/ice contact. This study, coupled with the body of work already available to the public audience should help in the decision process to select *in situ* burning as the means of oil spill response by further analyzing the details of a spill on ice. As mentioned, future studies will be required to answer the questions left open at the conclusion of this work and further vet the process of *in situ* burning of oil in an ice channel.

References

[1] N. K. Smith and A. Diaz, "In-place burning of crude oil in broken ice, 1985 testing at OHMSETT," in *Arctic and Marine Oil spill Program (AMOP) technical seminar*, 8th proceedings, (Edmonton, Alberta, Canada, Ottawa, Ontario), pp. 176 – 191, Environment Canada, 1985.

[2] N. K. Smith and A. Diaz, "In-place burning of Prudhoe Bay oil in broken ice: 1985 testing at OHMSETT," 1985. Proceedings of the 1985 Oil Spill Conference, API Publication No. 4385, American Petroleum Institute, Washington, D.C., 405-409 pp.

[3] N. K. Smith and A. Diaz, "In-place burning of crude oils in broken ice," 1987. Proceedings of the 1987 Oil Spill Conference, API Publication No. 4352, American Petroleum Institute, Washington, D.C., 483-387 pp.

[4] H. M. Brown and R. H. Goodman, "*In situ* burning of oil in ice leads," 1986. Arctic and Marine Oil spill Program (AMOP) technical seminar, 9th proceedings. 176-191 pp.

[5] I. A. Buist and D. F. Dickins, "Experimental spills of crude oil in pack ice," 1987. Proceedings of the 1987 Oil Spill Conference, API Publication No. 4352, American Petroleum Institute, Washington, D.C., 373-381 pp.

[6] P. Sveum, C. Bech, and M. Thommasen, "Burning oil in snow. experiments and implementation in a Norsk hydro drilling contingency plan," 1991. Arctic and Marine Oil spill Program (AMOP) technical seminar, 14th proceedings. 339-410 pp.

[7] C. Bech, P. Sveum, and I. Buist, "The effects of wind, ice and waves on the *in situ* burning of emulsions and aged oils," 1993. Arctic and Marine Oil spill Program (AMOP) technical seminar, 16th proceedings. 399-410 pp.

[8] C. Guennette and R. Wighus, "*In-situ* burning of crude oil and emulsions in broken ice," 1996. Arctic and Marine Oil spill Program (AMOP) technical seminar, 19th proceedings. 895-906 pp.

[9] I. A. Buist, "*In situ* burning of oil spills in ice and snow," 2000. Alaska Clean Seas.

[10] S. L. Ross Environmental Research Ltd, D. F. Dickins Associates Ltd, and Alaska Clean Seas, "Tests to determine the limits of *in situ* burning of thin oil slicks in broken ice," 2003. SL Ross Environemental Research Ltd and DF Dickins Associates Ltd and Alaska Clean Seas.

[11] A. Nilsson, "Arctic pollution issues: A state of the arctic environment report," tech. rep., Arctic Monitoring and Assessment Programme, 1997.

[12] A. Allen, "Contained controlled burning of spilled oil during the Exxon Valdez oil spill," 1990. Arctic and Marine Oil spill Program (AMOP) technical seminar, 9th Proceedings.

[13] Alaska Clean Seas, Pouch 340022, Prudhoe Bay, AK 99734-0022, *Technical Manual: Volume 1 Tactics Description*, June 2010.

[14] "Resource collection," in *In situ Burning of Oil Spills* (W. D. Walton, ed.), no. NIST SP 995, National Institute of Standards and Technology, 2003.

[15] National Response Team, *Bibliography on In-Situ Burning*, April 1998.

[16] J. P. Garo, J. P. Vantelon, S. Gandhi, and J. L. Torero, "Determination of thermal efficiency of preboilover burning of a slick on water," *Spill Science & Technology Bulletin*, vol. 5, pp. 141–151, 1999.

[17] J. L. Torero, S. M. Olenick, J. P. Garo, and J. P. Vantelon, "Determination of burning characteristics of a slick on water," *Spill Science & Technology Bulletin*, vol. 8, pp. 379–390, 1999.

[18] N. Wu, M. Baker, G. Kolb, and J. L. Torero, "Ignition, flame spread and mass burning characteristics of liquid fuels on a water bed," 1997. Arctic and Marine Oil spill Program (AMOP) technical seminar, 20th proceedings. 769-793 pp.

[19] N. Wu, G. Kolbe, and J. Torero, "The effect of weathering on the flammability of a slick of crude oil on a water bed," *Combustion Science and Technology*, vol. 161, pp. 269–308, 2000.

[20] J. A. Fay, "The spread of oil slicks on a calm sea," in *Oil on the Sea* (D. P. Hoult, ed.), Ocean Technology, (Cambridge, Massachussets), pp. 53 – 63, Massachusetts Institute of Technology and Woods Hole Oceanographic Institute, Plenum Press, May 1969. Proceedings of a Symposium on the Scientific and Engineering Aspects of Oil Pollution of the Sea.

[21] BP Lubricants USA inc., "466158-US12 US13, Castrol HD motor oil 30," 08/20/10. http:// www.castrol.com.

[22] EMD Chemicals, Inc., "PX0425 GR ACS petroleum ether," 09/21/10. http://www.emdchemicals.com.

[23] F. P. Incropera, D. P. Dewitt, T. L. Bergman, and A. S. Lavine, *Introduction to Heat Transfer, 5th edition*. John Wiley & Sons, 2007.

[24] H. E. Huppert, R. S. J. Sparks, J. S. Turner, and N. T. Arndt, "Emplacement and cooling of komatiite lavas," *Nature*, vol. 309, pp. 19 – 22, 1984.

[25] H. D. Ross, "Ignition of and flame spread over laboratory-scale pools of pure liquid fuels," *Prog. Energy Combust. Sci.*, vol. 20, pp. 17 – 63, 1994.

[26] D. D. Evans, "In-situ burning of oil spills," in *Alaska Arctic Offshore Oil Spill Response Technology Workshop Proceedings* (N. H. Jason, ed.), no. National Institute of Standards and Technology Special Publications 792, National Institute of Standards and Technology, 1989.

[27] H. E. Huppert, "The propagation of two-dimensional and axisymmetric viscous gravity currents over a rigid horizontal surface," *J. Fluid Mech.*, vol. 121, pp. 43–58, 1982.

[28] Petroleum Naphtha, "CAMEO Chemicals," June 1999. http:// cameochemicals. noaa.gov /chris/PTN.pdf.

[29] M. Ungarish, *An Introduction to Gravity Currents and Intrusions*. Boca Raton, FL, USA: CRC Press, 2009.

[30] R. Hibbler, *Mechanics of Materials*. Pearson Prentice Hall, 2005.

Appendix A

Mass Loss Rate Appendix

Figure A.1 provides the raw data for the 1 cm trials; Eq. A.1, A.2 and A.3 correspond to fig. A.1a, fig. A.1b and fig. A.1c, respectively. For the purposes of recreating the data set these equations have been represented in there raw form.

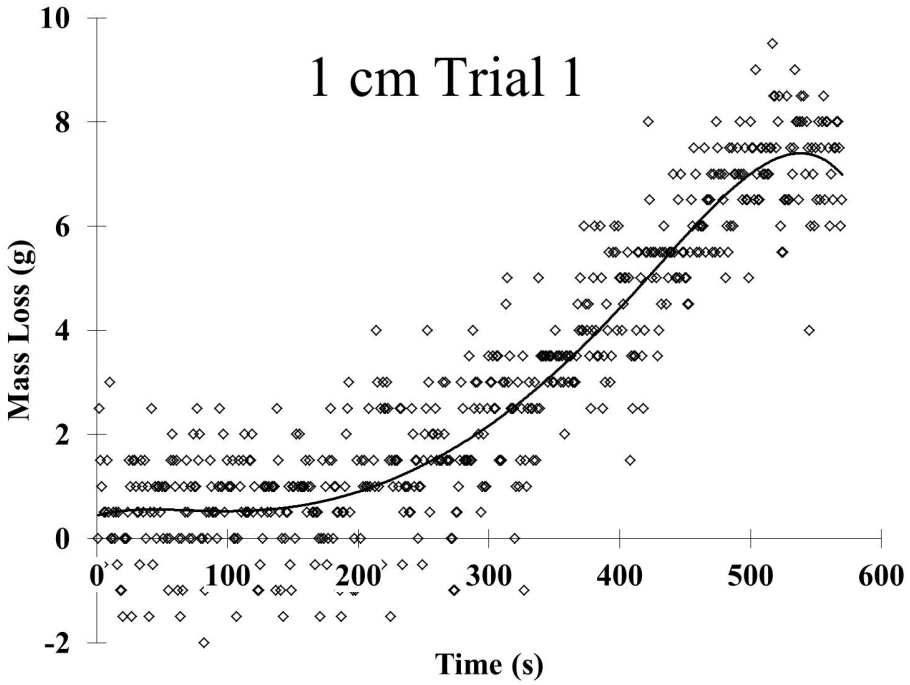

(a)

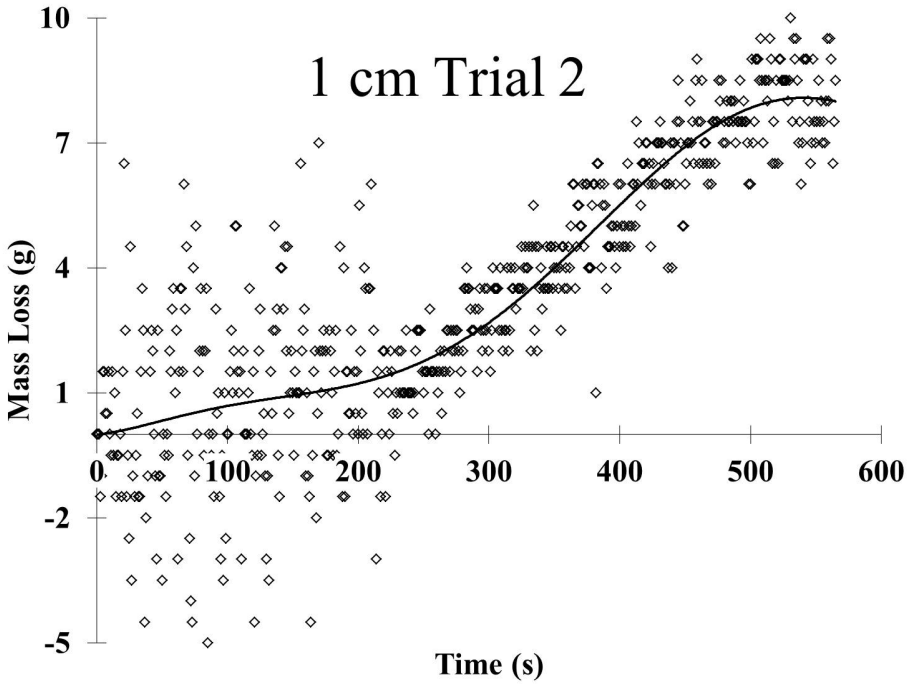

(b)

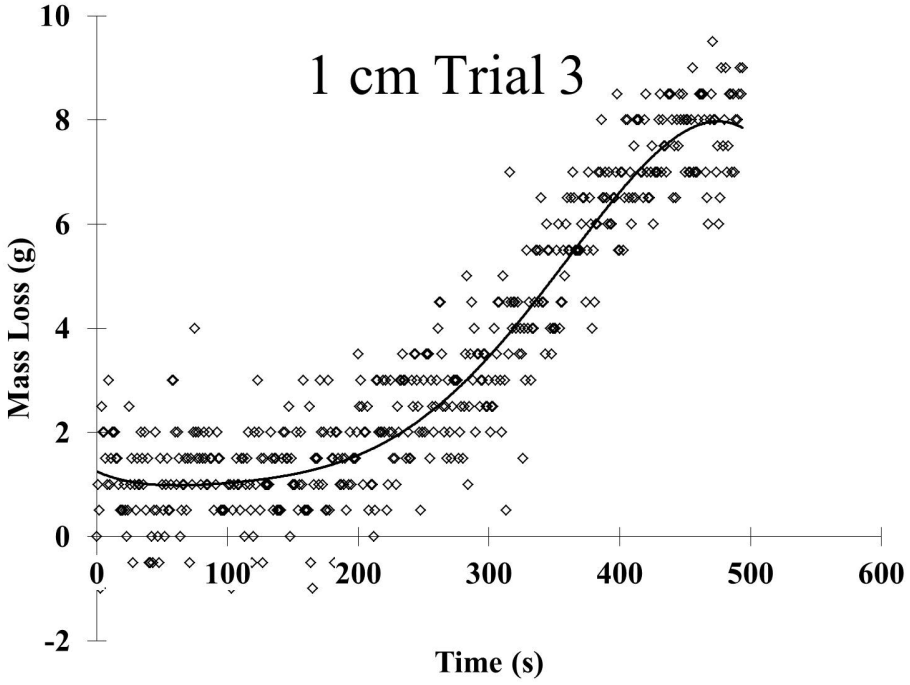

(c)

Figure A.1: Mass loss data for the 1 cm trial fitted to a 6th-order polynomial. These trendlines are differentiated to obtain a mass loss rate.

1 cm channel width trial 1 mass loss trendline equation

$$\begin{aligned} dM = &-3.79624462041059 \times 10^{-15} t^6 + 5.52671240548817 \times 10^{-12} t^5 \\ &- 3.28076055755138 \times 10^{-9} t^4 + 1.03052677736447 \times 10^{-6} t^3 \\ &- 1.3631446572493 \times 10^{-4} t^2 + 6.96171382287782 \times 10^{-3} t \\ &+ 4.41905788043717 \times 10^{-1} \\ r^2 = &\ 0.86 \end{aligned} \tag{A.1}$$

1 cm channel width trial 2 mass loss trendline equation

$$\begin{aligned} dM = &\ 5.23778934127943 \times 10^{-15} t^6 - 9.21560095343437 \times 10^{-12} t^5 \\ &+ 5.54065857679819 \times 10^{-9} t^4 - 1.31203511866129 \times 10^{-6} t^3 \\ &+ 1.20142527730849 \times 10^{-4} t^2 + 3.3317215684292 \times 10^{-3} t \\ &- 2.99346052815963 \times 10^{-3} \\ r^2 = &\ 0.76 \end{aligned} \tag{A.2}$$

1 cm channel width trial 3 mass loss trendline equation

$$\begin{aligned} dM = &\ 3.46344025048179 \times 10^{-15} t^6 - 7.28162364372541 \times 10^{-12} t^5 \\ &+ 4.74479837332068 \times 10^{-9} t^4 - 1.23933973666945 \times 10^{-6} t^3 \\ &+ 1.76240524780269 \times 10^{-4} t^2 - 1.15170519102321 \times 10^{-2} t \\ &+ 1.25371190884653 \\ r^2 = &\ 0.89 \end{aligned} \tag{A.3}$$

Figure A.2 provides the raw data for the 2 cm channel width trials; Eq. A.4, A.5 and A.6 correspond to fig. A.2a, fig. A.2b and fig. A.2c, respectively. For the purposes of recreating the data set these equations have been represented in there raw form. Inconstancies in channel formation resulted in trial 2 having approximately twice the mass of fuel as trial 1 or 3. This corresponded directly to a doubling of the amount of consumed fuel in the same duration of time.

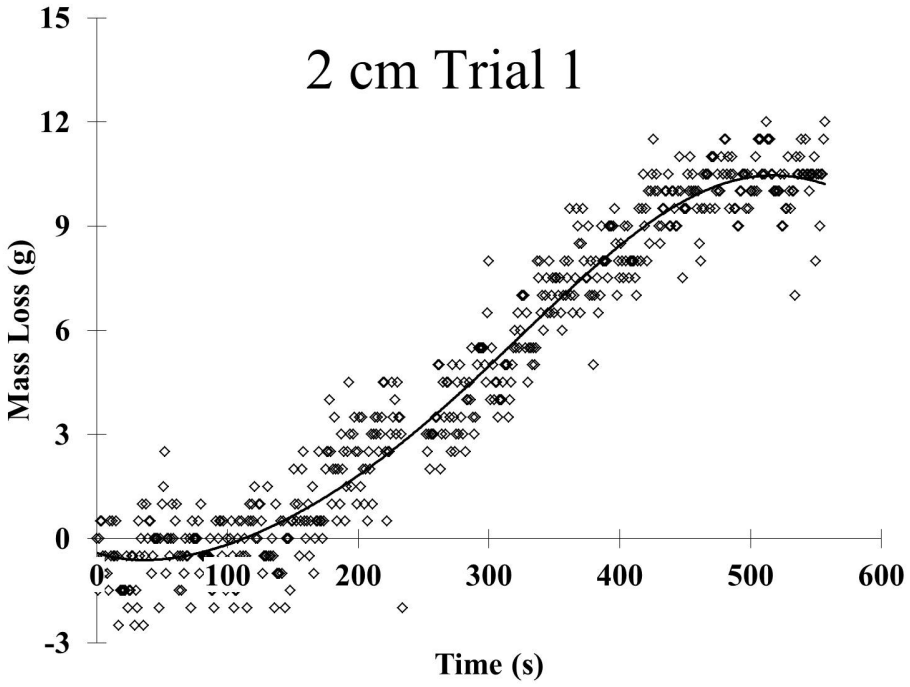
2 cm Trial 1
Mass Loss (g)
Time (s)
15
12
9
6
3
0
-3
0
100
200
300
400
500
600

(a)

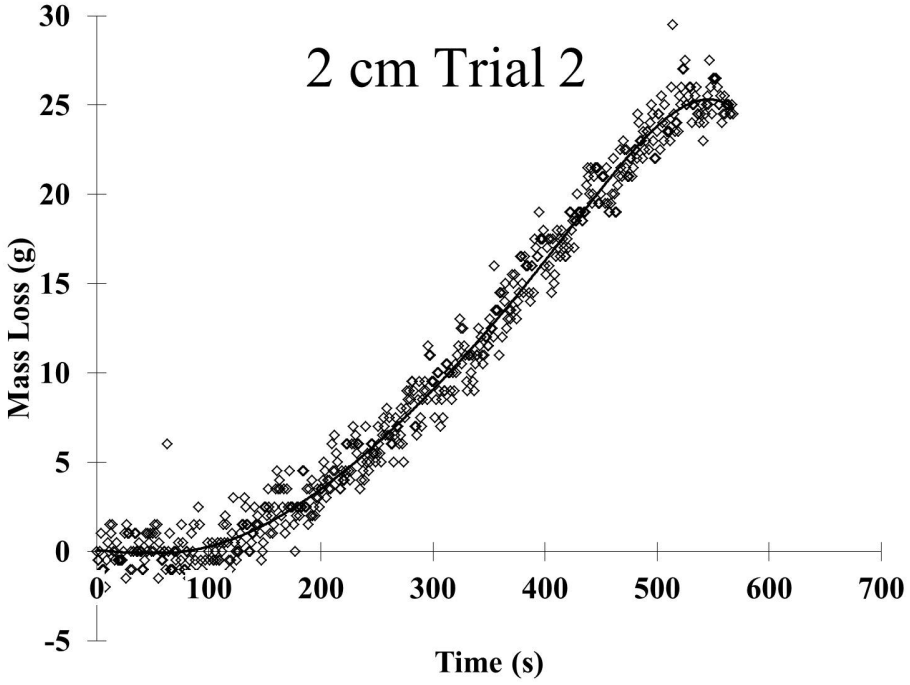
2 cm Trial 2
Mass Loss (g)
Time (s)
30
25
20
15
10
5
0
-5
0
100
200
300
400
500
600
700

(b)

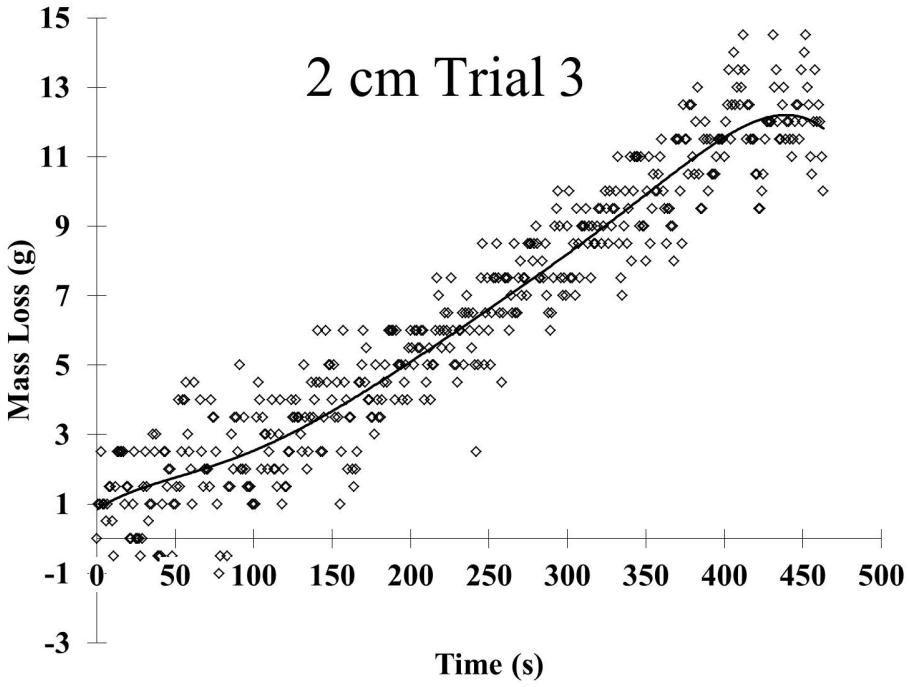

(c)

Figure A.2: Mass loss data for the 2 cm trials fitted to a 6th-order polynomial.

2 cm channel width trial 1 mass loss trendline equation

$$\begin{aligned} dM = {} & 2.82637607737107 \times 10^{-15} t^6 - 4.81689512313691 \times 10^{-12} t^5 \\ & + 2.86710775368633 \times 10^{-09} t^4 - 8.67311591129516 \times 10^{-7} t^3 \\ & + 2.10349562610901 \times 10^{-4} t^2 - 1.23659005203081 \times 10^{-2} t \\ & - 4.0791180161068 \times 10^{-1} \\ r^2 = {} & 0.95 \end{aligned} \tag{A.4}$$

2 cm channel width trial 2 mass loss trendline equation

$$\begin{aligned} dM = {} & -1.00620686177648 \times 10^{-14} t^6 + 1.45732818847596 \times 10^{-11} t^5 \\ & - 8.04572460998826 \times 10^{-9} t^4 + 1.97862743861466 \times 10^{-6} t^3 \\ & - 6.70004879097519 \times 10^{-5} t^2 - 4.34783902073832 \times 10^{-3} t \\ & + 7.78651857108343 \times 10^{-2} \\ r^2 = {} & 0.99 \end{aligned} \tag{A.5}$$

2 cm channel width trial 3 mass loss trendline equation

$$\begin{aligned} dM = &-4.08236219609258 \times 10^{-15} t^6 + 5.77663045973999 \times 10^{-12} t^5 \\ &- 3.2311326689325 \times 10^{-9} t^4 + 7.61815745098371 \times 10^{-7} t^3 \\ &+ 9.31101067891404 \times 10^{-6} t^2 - 2.6239252324558 \times 10^{-3} t \\ &- 5.16794879215013 \times 10^{-1} \\ r^2 = &\ 0.95 \end{aligned} \tag{A.6}$$

The raw data the the first two trials in the 4 cm channel width data set. The third trial is presented in the body of the document and is not shown here. However, equations A.7, A.8 and A.9 correspond to fig. A.3a, fig. A.3b and fig. 2.2 respectively. For the purposes of recreating the data set these equations have been represented in there raw form. Equation A.9 and eq. 2.1 are idential expect for the number of significant figures shown.

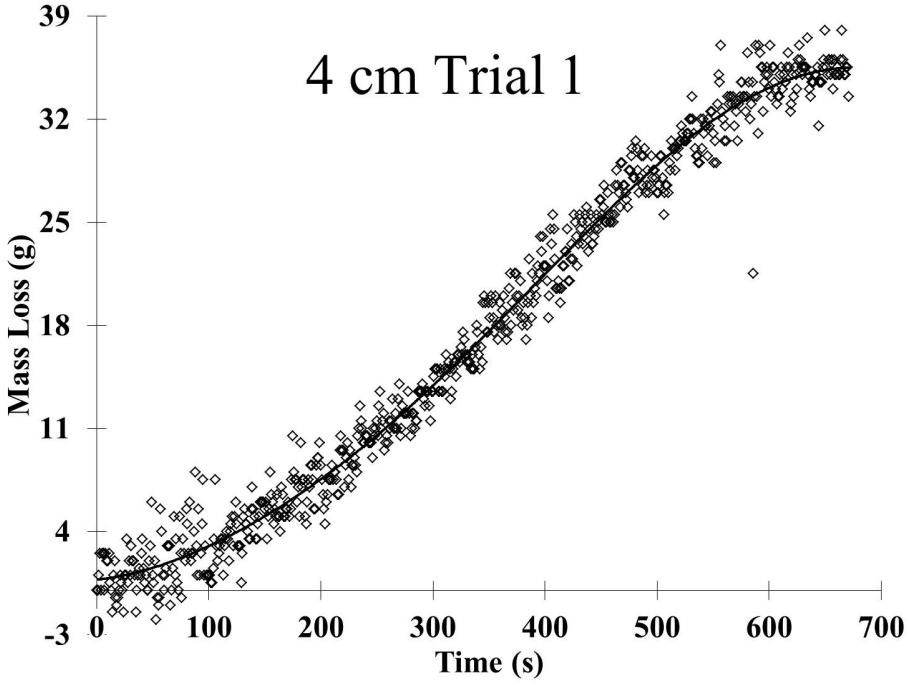

(a)

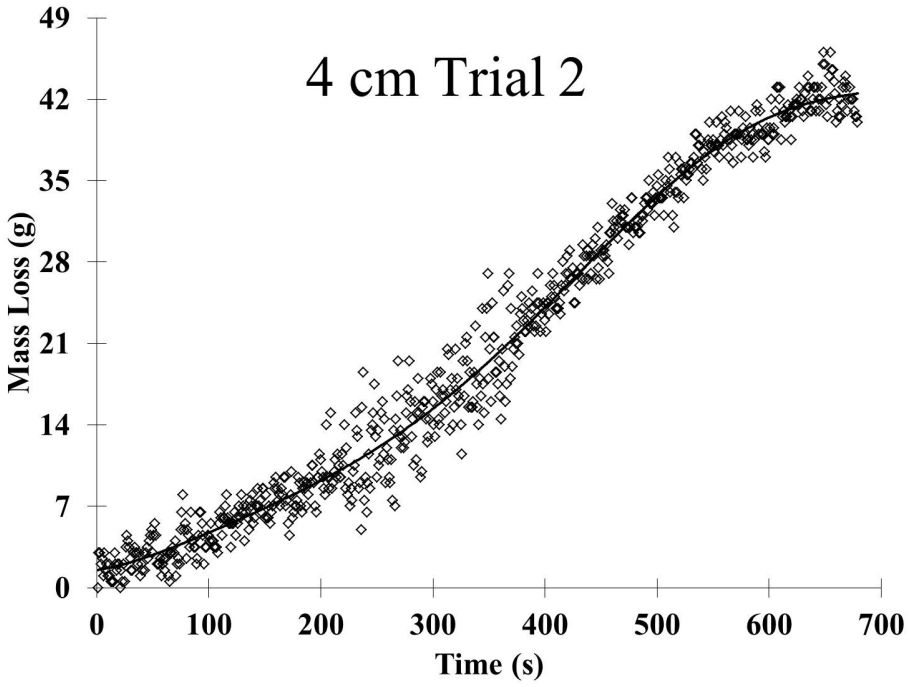

(b)

Figure A.3: Mass loss data for the 4 cm trials fitted to a 6th-order polynomial. Equations A.7, and A.8 correspond to figures a and b, respectively.

4 cm channel width trial 1 mass loss trendline equation

$$\begin{aligned} dM = {} & 1.02347341079572 \times 10^{-15} t^6 - 2.06700523379719 \times 10^{-12} t^5 \\ & + 1.34813793472872 \times 10^{-9} t^4 - 4.60664337287309 \times 10^{-7} t^3 \\ & + 1.84585129666459 \times 10^{-4} t^2 + 7.85461820441924 \times 10^{-3} t \\ & + 7.30213793955045 \times 10^{-1} \\ r^2 = {} & 0.99 \end{aligned} \tag{A.7}$$

4 cm channel width trial 2 mass loss trendline equation

$$\begin{aligned} dM = {} & 4.79486950652837 \times 10^{-15} t^6 - 9.62468495597672 \times 10^{-12} t^5 \\ & + 6.67813908420166 \times 10^{-9} t^4 - 1.96075067168615 \times 10^{-6} t^3 \\ & + 3.13480342518065 \times 10^{-4} t^2 + 1.46959140054121 \times 10^{-2} t \\ & + 1.51573344832707 \\ r^2 = {} & 0.99 \end{aligned} \tag{A.8}$$

4 cm channel width trial 3 mass loss trendline equation

$$\begin{aligned} dM = {} & 6.09754908884717 \times 10^{-15} t^6 - 1.15468993530685 \times 10^{-11} t^5 \\ & + 7.41379176365936 \times 10^{-9} t^4 - 1.90298686369994 \times 10^{-6} t^3 \\ & + 2.58666873705238 \times 10^{-4} t^2 + 2.89396192501954 \times 10^{-2} t \\ & + 3.22703637127415 \\ r^2 = {} & 0.98 \end{aligned} \tag{A.9}$$

1 cm channel width trial 1 mass loss rate equation

$$\begin{aligned} \frac{dM}{dt} = {} & -2.27774677224635 \times 10^{-14} t^5 + 2.76335620274408 \times 10^{-11} t^4 - 1.31230422302055 \times 10^{-8} t^3 \\ & + 3.09158033209341 \times 10^{-6} t^2 - 0.00027262893144986 t + 0.00696171382287782 \end{aligned} \tag{A.10}$$

1 cm channel width trial 2 mass loss rate equation

$$\begin{aligned} \frac{dM}{dt} = {} & 3.14267360476766 \times 10^{-14} t^5 - 4.60780047671719 \times 10^{-11} t^4 + 2.21626343071928^{-8} t^3 \\ & - 3.93610535598387 \times 10^{-6} t^2 + 0.00024028505546169 8t + 0.0033317215684292 \end{aligned} \tag{A.11}$$

1 cm channel width trial 3 mass loss rate equation

$$\begin{aligned} \frac{dM}{dt} = {} & 2.07806415028907 \times 10^{-14} t^5 - 3.64081182186271^{-11} t^4 + 1.89791934932827^{-8} t^3 \\ & - 3.71801921000835 \times 10^{-6} t^2 + 0.000352481049560538 t - 0.0115170519102321 \end{aligned} \tag{A.12}$$

2 cm channel width trial 1 mass loss rate equation

$$\begin{aligned} \frac{dM}{dt} = {} & 1.69582564642264 \times 10^{-14} * t^5 - 2.40844756156846 \times 10^{-11} * t^4 + 1.14684310147453 \times 10^{-8} * t^3 \\ & - 2.60193477338855 \times 10^{-6} * t^2 + 0.000420699125221802 * t - 0.0123659005203081 \end{aligned} \tag{A.13}$$

2 cm channel width trial 2 mass loss rate equation

$$\begin{aligned} \frac{dM}{dt} = {} & -6.03724117065888 \times 10^{-14} * t^5 + 7.2866409423798 \times 10^{-11} * t^4 - 3.2182898439953 \times 10^{-8} * t^3 \\ & + 5.93588231584398 \times -6 * t^2 - 0.000134000975819504 * t - 0.00434783902073832 \end{aligned} \tag{A.14}$$

2 cm channel width trial 3 mass loss rate equation

$$\frac{dM}{dt} = -5.22908127288168 \times 10^{-14} * t^5 + 5.91634230948595 \times 10^{-11} * t^4 - 2.38481379739516 \times 10^{-8} * t^3 + 3.80272122466053 \times 10^{-6} * t^2 - 0.0000586870521175342 * t - 0.00243164557400632 \tag{A.15}$$

4 cm channel width trial 1 mass loss rate equation

$$\frac{dM}{dt} = 6.14084046477432 \times 10^{-15} * t^5 - 1.03350261689859 \times 10^{-11} * t^4 + 5.39255173891488 \times 10^{-9} * t^3 - 1.38199301186193 \times 10^{-6} * t^2 + 3.69170259332918 \times 10^{-4} * t + 7.85461820441924 \times 10^{-3} \tag{A.16}$$

4 cm channel width trial 2 mass loss rate equation

$$\frac{dM}{dt} = 2.87692170391702 \times 10^{-14} * t^5 - 4.81234247798836 \times 10^{-11} * t^4 + 2.67125563368066 \times 10^{-8} * t^3 - 5.88225201505845 \times 10^{-6} * t^2 + 6.2696068503613 \times 10^{-4} * t + 1.46959140054121 \times 10^{-3} \tag{A.17}$$

4 cm channel width trial 3 mass loss rate equation

$$\frac{dM}{dt} = 3.6585294533083 \times 10^{-14} * t^5 - 5.77344967653425 \times 10^{-11} * t^4 + 2.96551670546374 \times 10^{-8} * t^3 - 5.70896059109982 \times 10^{-6} * t^2 + 5.17333747410476 \times 10^{-4} * t + 2.89396192501954 \times 10^{-2} \tag{A.18}$$

Petroleum Ether 1 cm channel width trial mass loss trendline equation

$$dM = -2.17719257999852 \times 10^{-11} t^6 + 1.47721812692879 \times 10^{-8} t^5 - 3.66329727541359 \times 10^{-6} t^4 + 4.12528729214046 \times 10^{-4} t^3 - 2.09199415061789 \times 10^{-2} t^2 + 4.31468313296136 \times 10^{-1} t - 2.5440837206952 \times 10^{-1} \tag{A.19}$$

$r^2 = 0.98$

Foil Lined 4 cm channel width trial mass loss trendline equation

$$dM = -5.38911763557722 \times 10^{-19}t^6 + 1.01499097007552 \times 10^{-14}t^5 - 5.1233238995246 \times 10^{-11}t^4 + 1.13673329853181 \times 10^{-7}t^3 - 1.32292480484963 \times 10^{-4}t^2 + 1.19923653735441 \times 10^{-1}t - 2.67724822739547 \quad \text{(A.20)}$$

$$r^2 = 0.99$$

Petroleum Ether 1 cm channel width trial mass loss rate equation

$$dM = -1.30631554799911 \times 10^{-10}t^5 + 7.38609063464395 \times 10^{-8}t^4 - 1.46531891016544 \times 10^{-5}t^3 + 1.23758618764214 \times 10^{-3}t^2 - 4.18398830123578 \times 10^{-2}t + 4.31468313296136 \times 10^{-1} \quad \text{(A.21)}$$

Foil Lined 4 cm channel width trial mass loss rate equation

$$dM = -3.23347058134633 \times 10^{-18}t^5 + 5.0749548503776 \times 10^{-14}t^4 - 2.0493295598098 \times 10^{-10}t^3 + 3.41019989559543 \times 10^{-7}t^2 - 2.64584960969926 \times 10^{-4}t + 1.19923653735441 \times 10^{-1} \quad \text{(A.22)}$$

Figure A.4 provides the remaining 10 second moving average thermocouple measurements of the 1 cm channel width data set. Figure A.4 is presented in the body of the document.

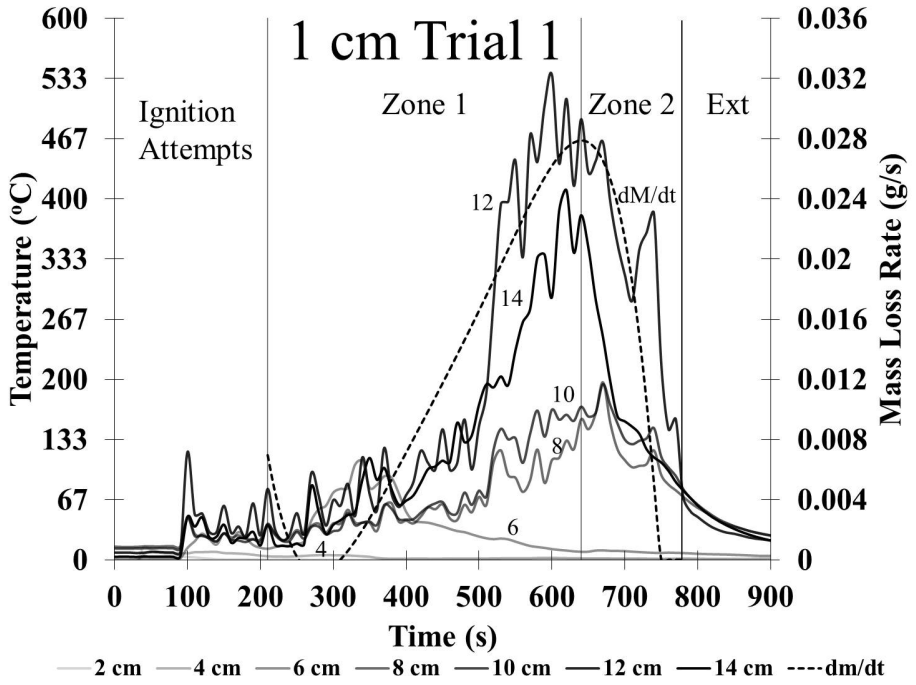

(a)

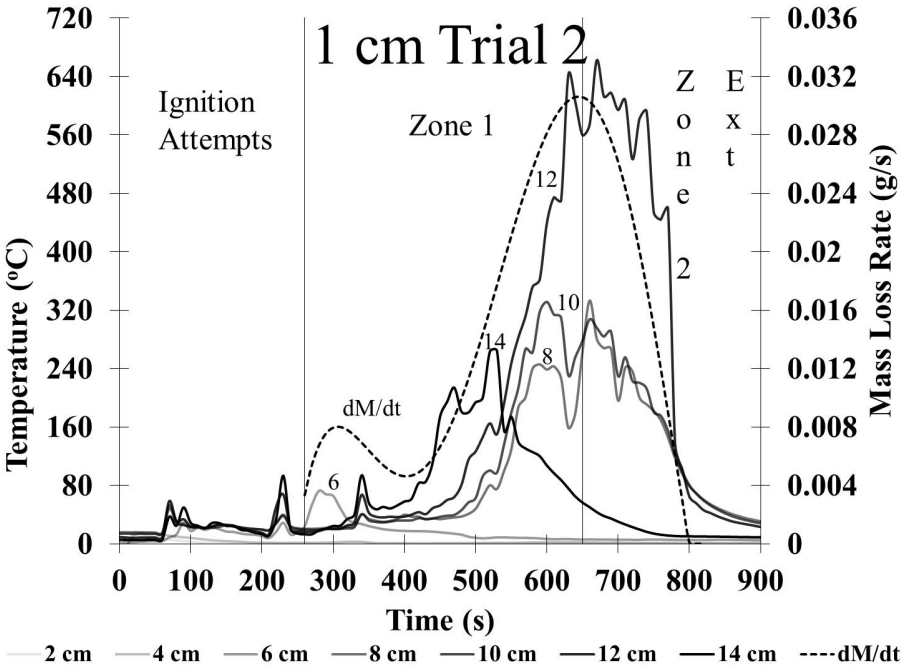

(b)

Figure A.4: The 10 second moving average plot of the temperature for trial 1 and trial 2 of the 1 cm channel width.

Figure A.5 provides the remaining 10 second moving average thermocouple measurements of the 2 cm channel width data set. Figure A.5 is presented in the body of the document.

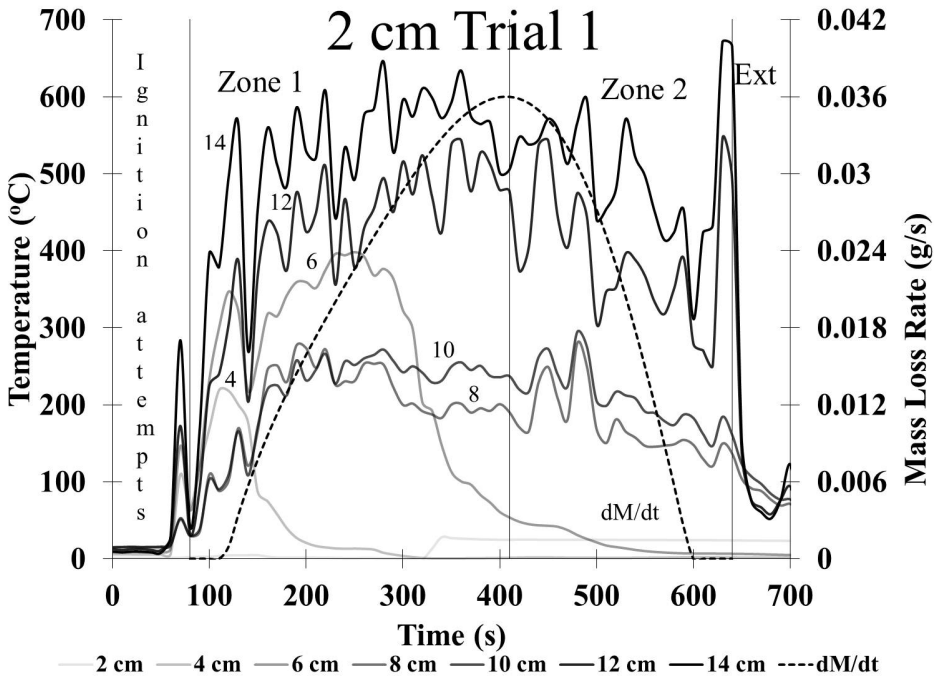

(a)

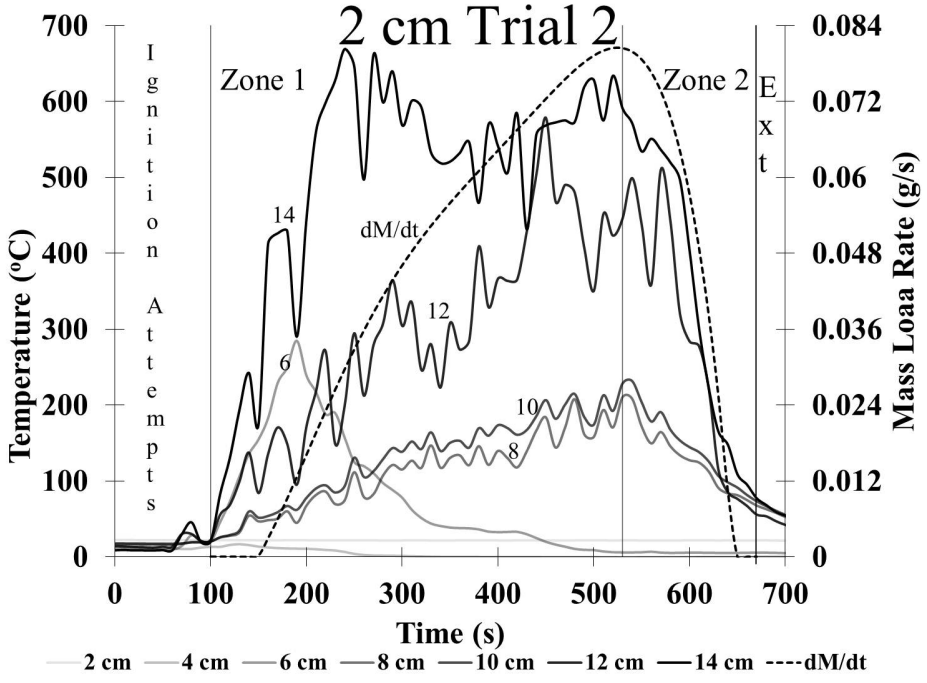

(b)

Figure A.5: The 10 second moving average plot of the temperature of trial 1 and trial 2 of for the 2 cm channel width

Figure A.6 provides the remaining temperature profiles of the 1 cm channel width data set.

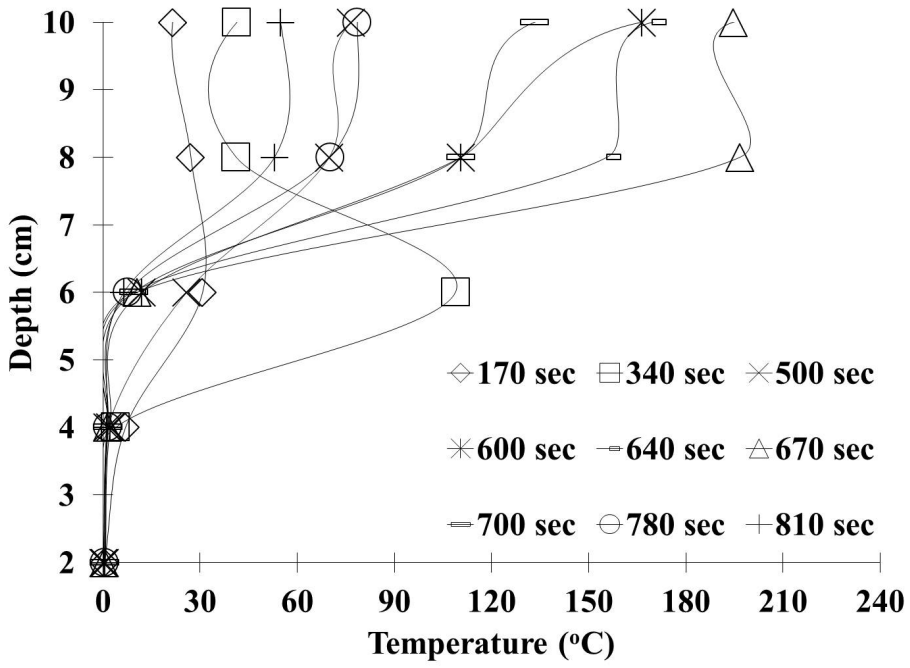

(a)

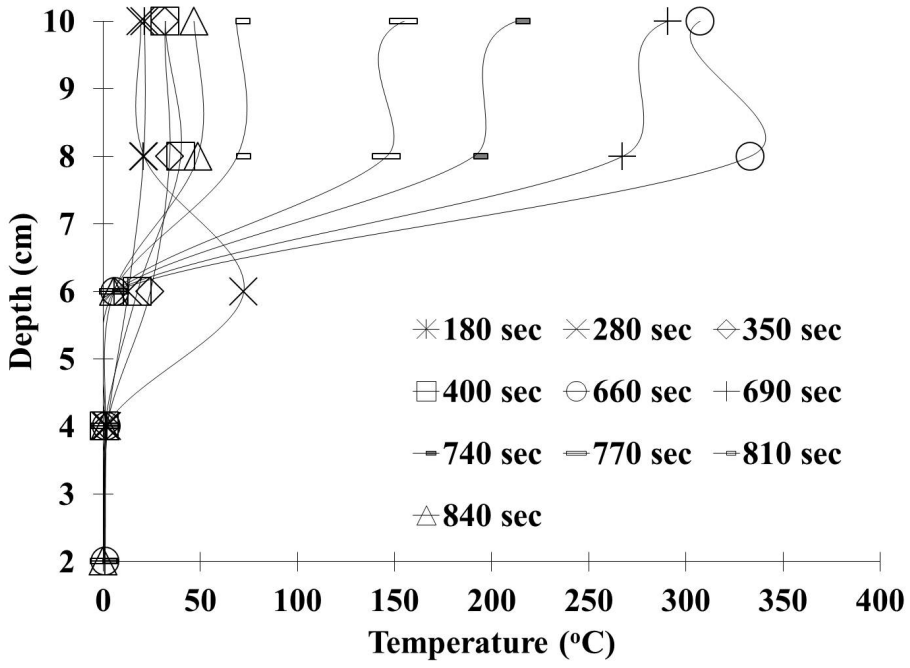

(b)

Figure A.6: The temperature profile of trial 1 and trial 2 for the 1 cm channel width

Figure A.7 provides the remaining temperature profiles of the 2 cm channel width data set.

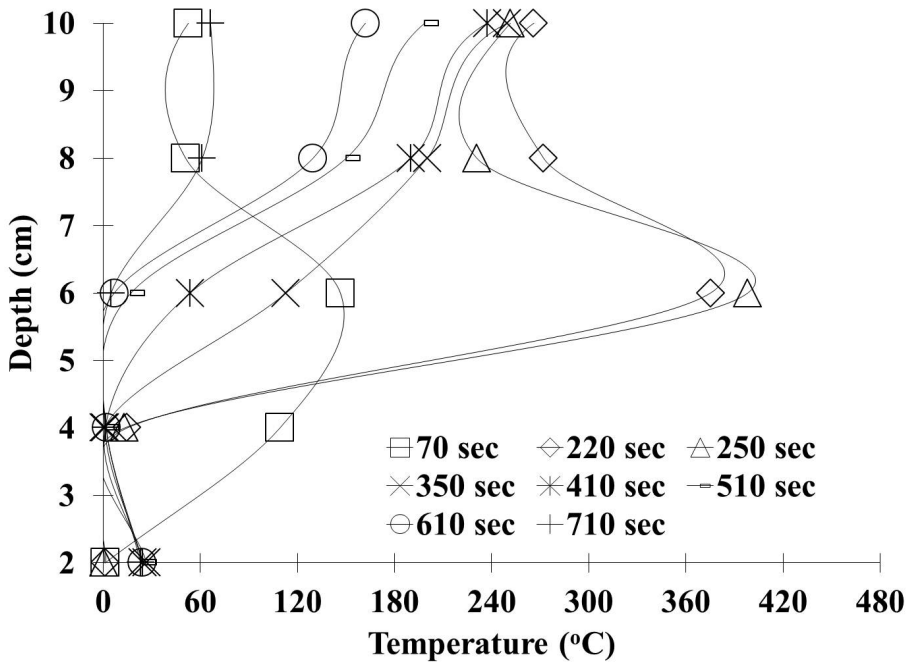

(a)

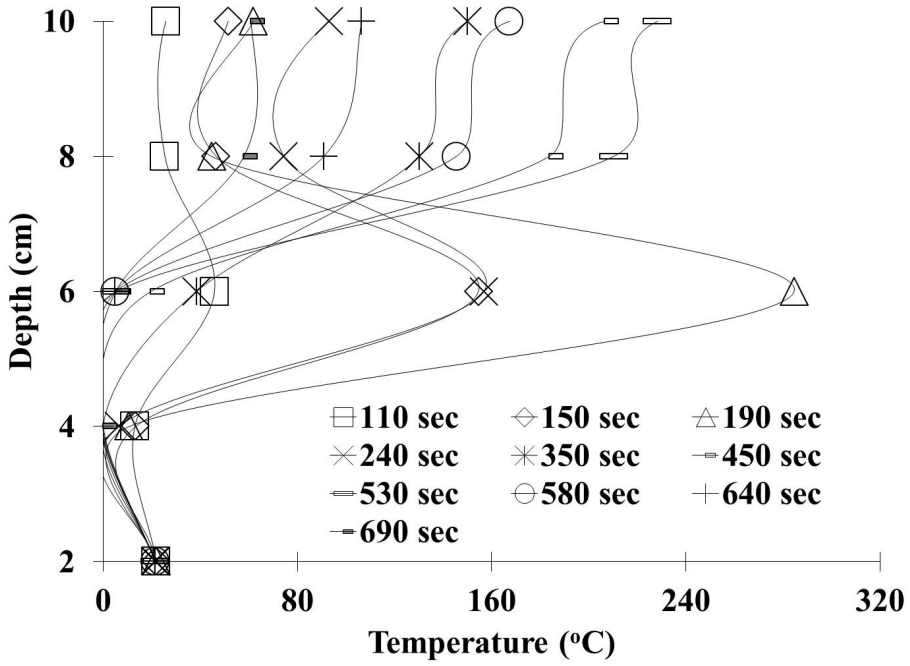

(b)

Figure A.7: The temperature profile of trial 1 and trial 2 for the 2 cm channel width

	1 cm	2 cm	4 cm	Foil	Petro Ether
Ignition Attempts	5	2	1	1	1
Time to Sustained Flame (s)	30	120	0	0	0
Time to Channel Wall Melt (s)	120	0	45	N/A	150
Time to Extinction (s)	690	570	660	2160	240
Final Duration (s)	510	540	660	2160	240

Presented here is a table with some observations of the study which were not discussed in the body of the document but still provide insight and assisted analysis.

Table A.1: Maximum Temperature (^{o}C) Summary

	2 cm	4 cm	6 cm	8 cm	10 cm	12cm	14cm
1 cm	14	13	77	313	322	652	302
2 cm	24	90	35	230	244	559	688
4 cm	8	57	467	416	405	791	780

Table A.2: Fuel Layer Measurements

		1 cm	2 cm	4 cm	Foil
Initial Mass	g	86	155	342	240
Initial Volume	ml	112	202	446	312
Initial Depth	cm	2.8	2.5	2.8	2.0
Final Mass	g	77	138	301	151
Final Diameter	cm	6.8	9.3	16.7	4.0
Final Area	cm^2	250	333	491	160
Final Depth	cm	0.4	0.5	0.8	1.2
Final Volume	ml	100	180	392	197
Duration	s	510	540	660	2130
Efficiency	%	10	10	12	37

Table A.3: Ice Melt Data

	1 cm	2 cm	4 cm
Volume (ml)	660	1120	1600
% Increase	265	240	200
Net Heat Loss (kW)	0.3	0.5	0.6

Table A.4: Ice Lip Characteristics (cm)

cm	1 cm		2 cm		4 cm	
	Left	Right	Left	Right	Left	Right
Undercut Thickness	1.4	1.5	1.7	1.2	1.7	1.2
Undercut Penetration	0.2	0.5	0.7	0.3	1.8	1.0
Lip Thickness	1.1	1.0	1.3	1.2	1.2	0.5

The following photographs are a presented to provide the reader with an appreciation of the work and perhaps assist in future research endeavors.

Figure A.8: Example of Oil Over Flow from Channel: Side View

Figure A.9: Example of Oil Over Flow from Channel: Side View

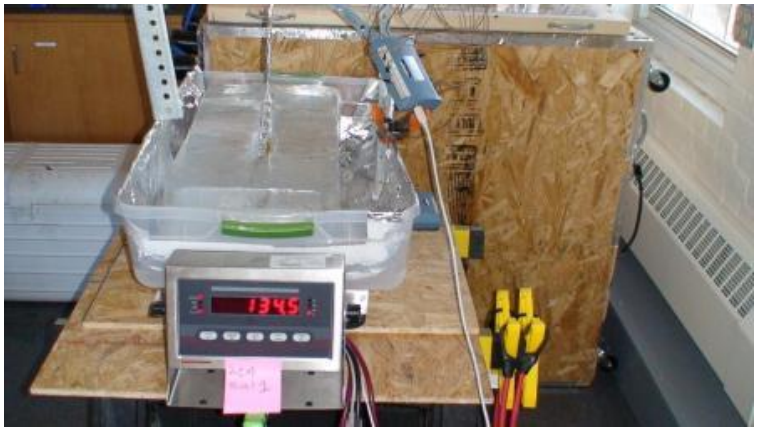

Figure A.10: 2 cm Trial 1 set up

Figure A.11: 2 cm trial 1 overflow

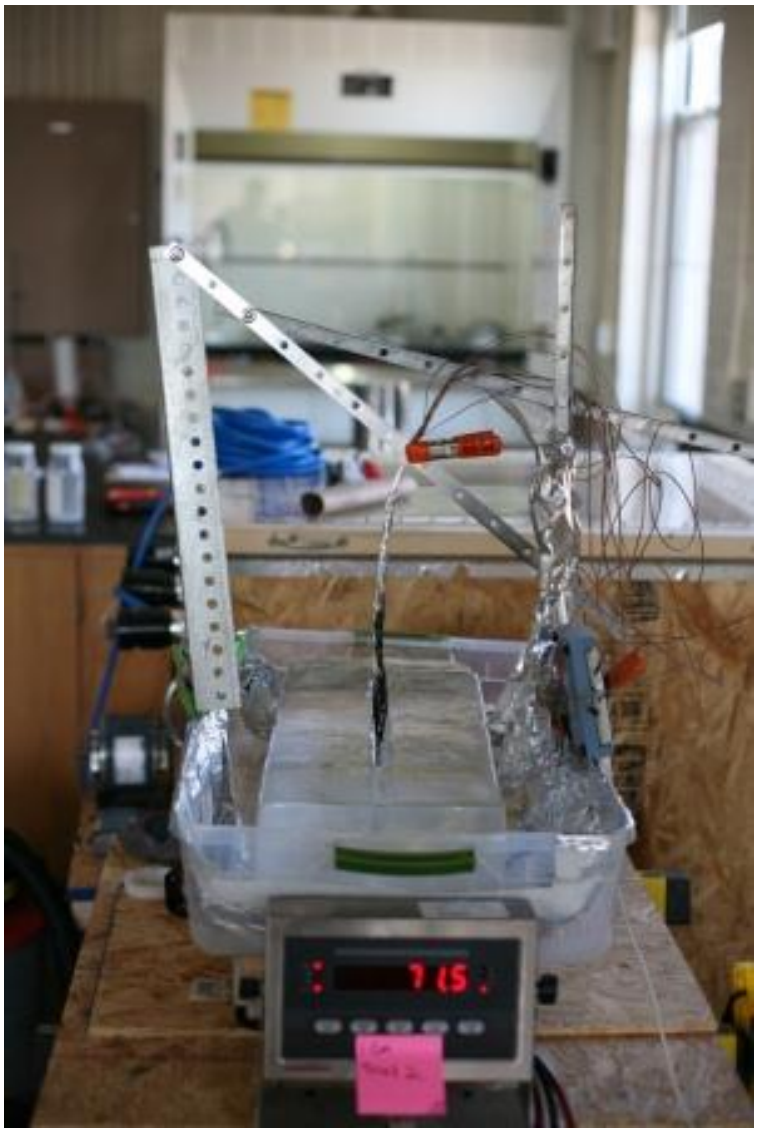

Figure A.12: 1 cm Trial 2 Set Up

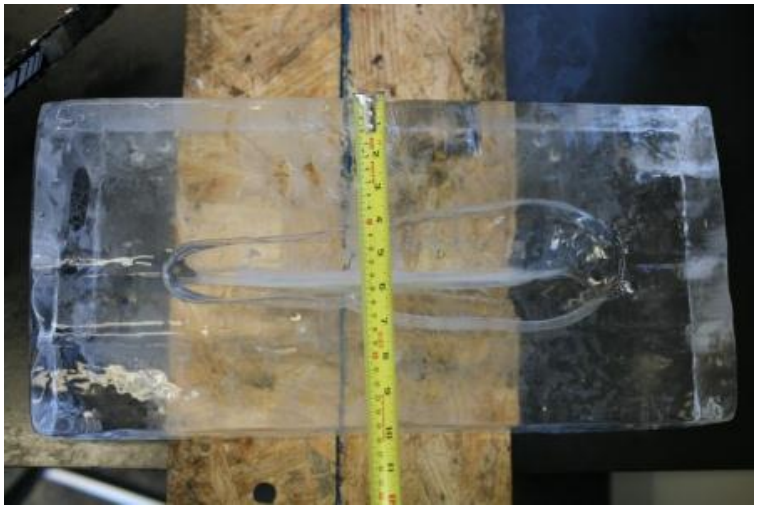

Figure A.13: 1 cm Trial 2 Final Channel Size

Figure A.14: Foil Trial: Preliminary Set-up

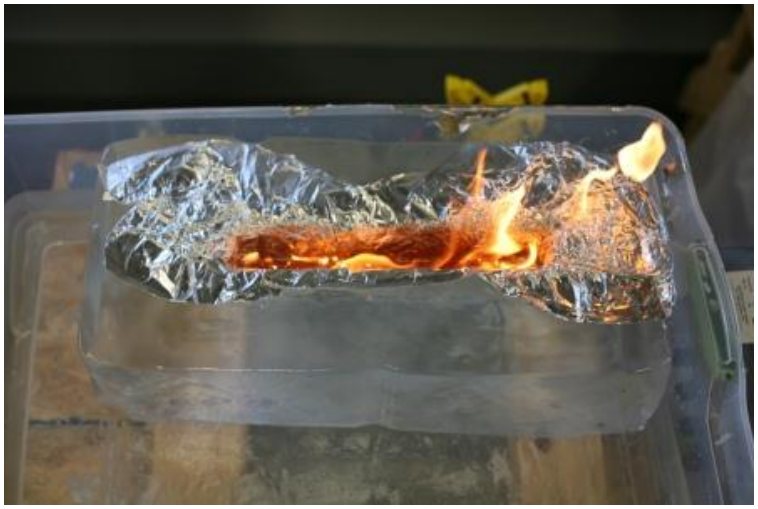

Figure A.15: Foil Trial: Top View

Figure A.16: Foil Trial: Side View

Figure A.17: Foil Trial: Mid-burn Top View

Figure A.18: Foil Trial: Mod-Burn Side View

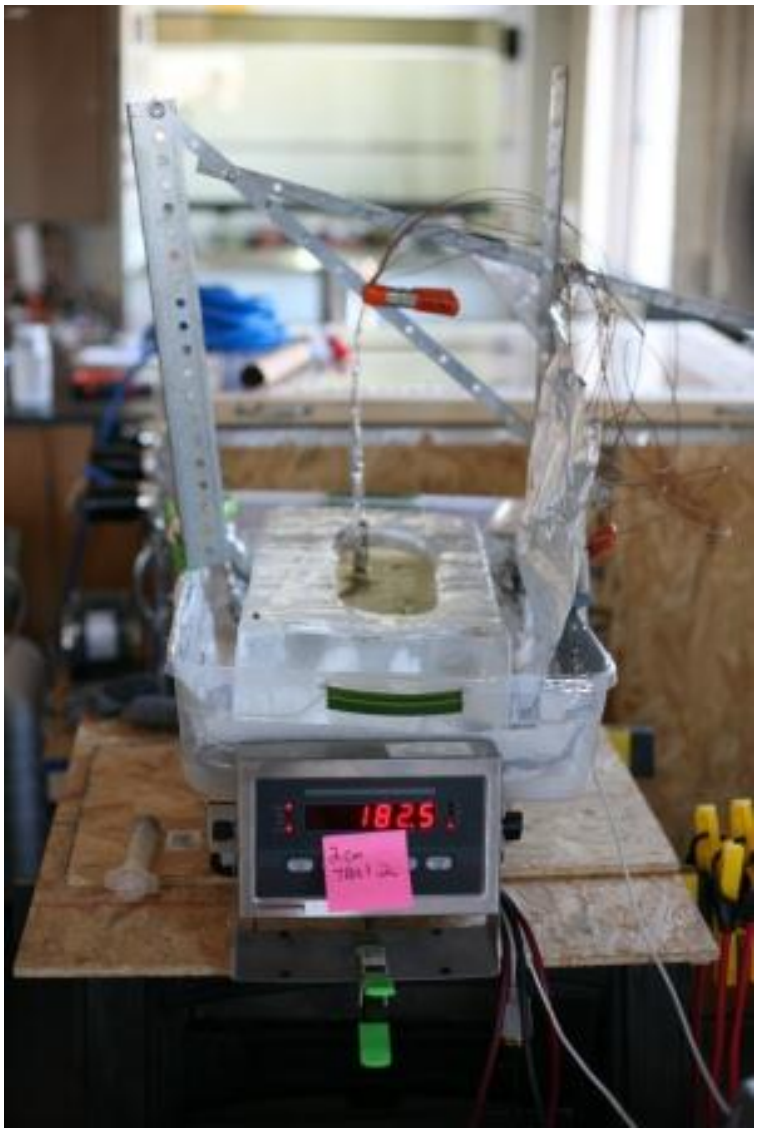

Figure A.19: 2 cm Trial 2: Final

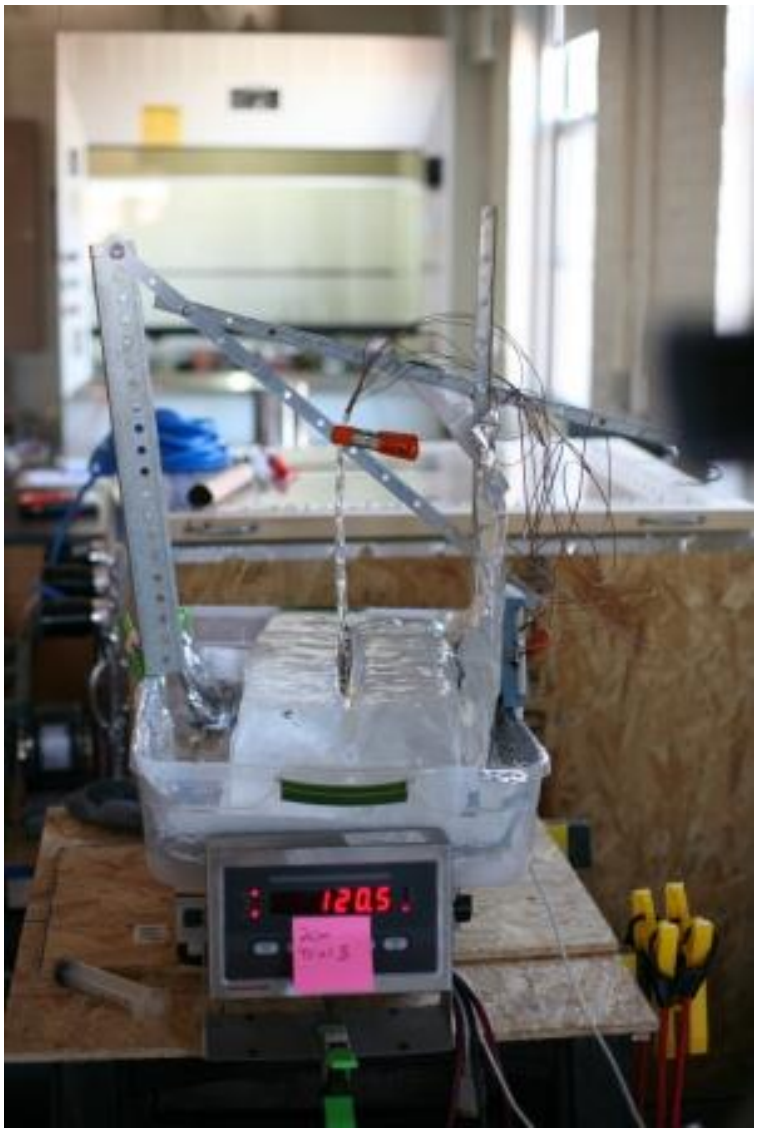

Figure A.20: 2 cm Trial 3: Preliminary Set-up

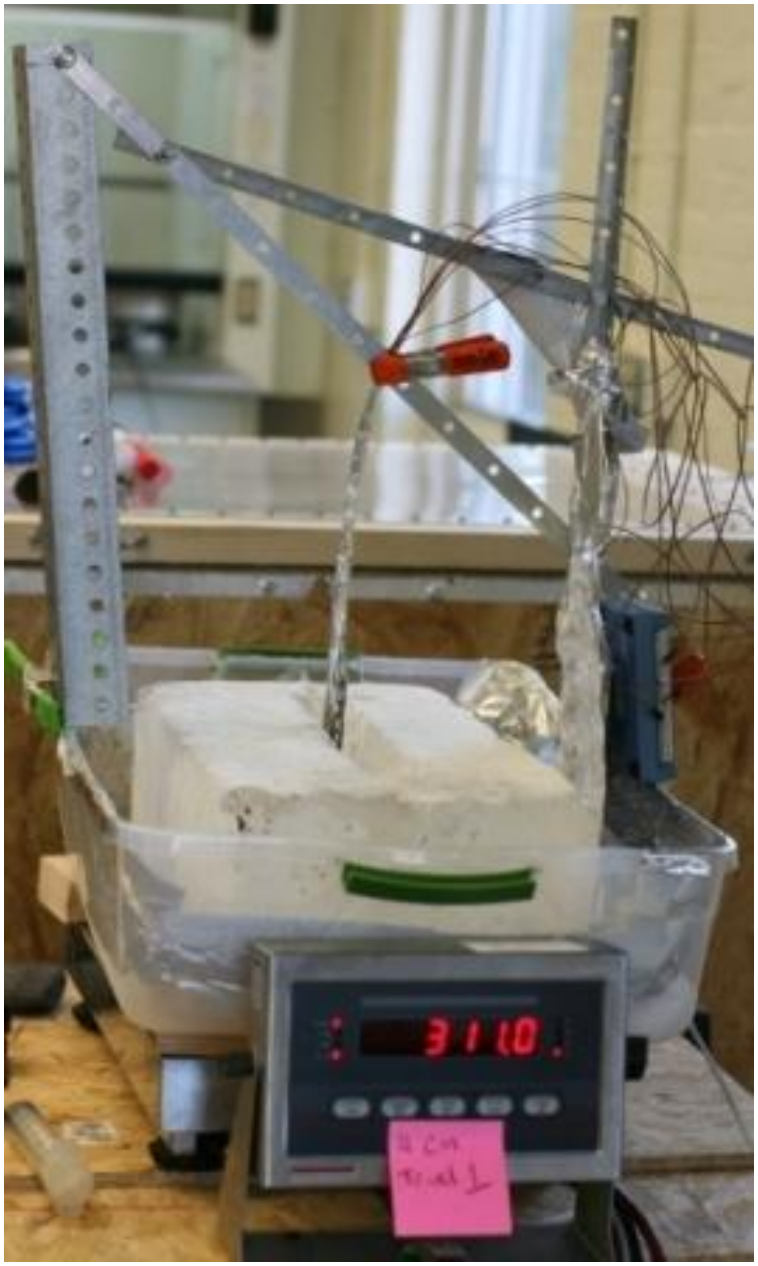

Figure A.21: 4 cm Trial 1: Preliminary Set-up

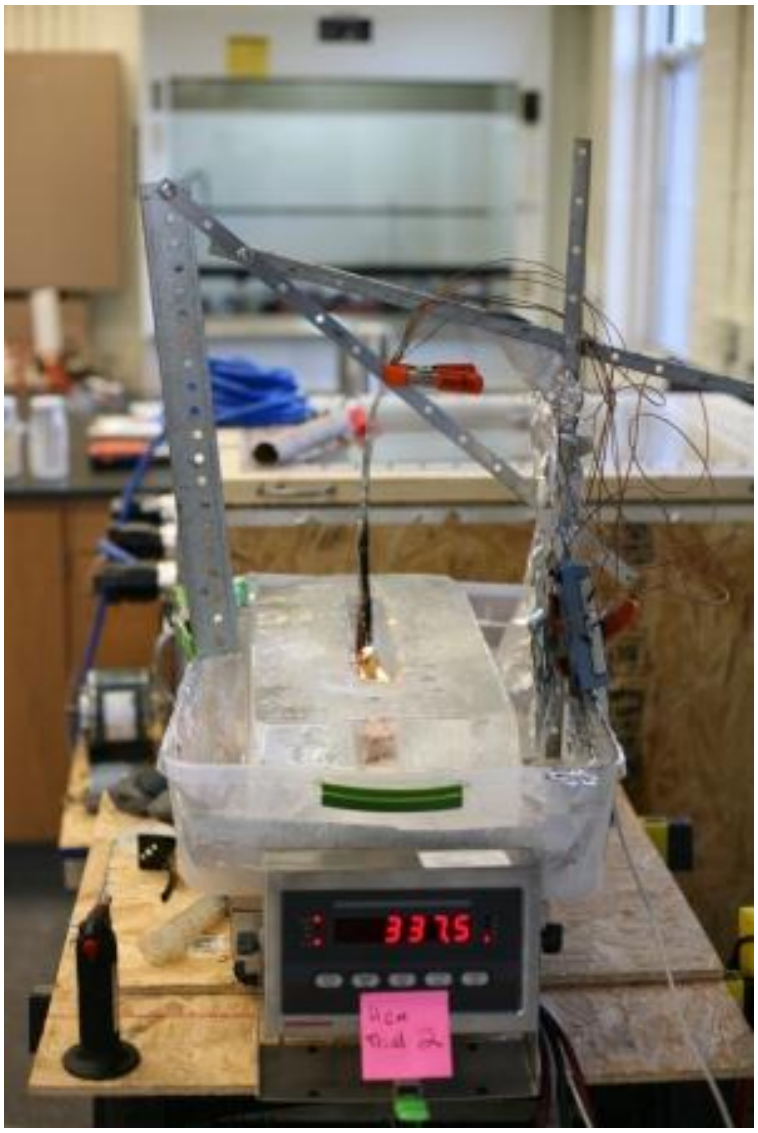

Figure A.22: 4 m Trial 2: Zone 1 of burning

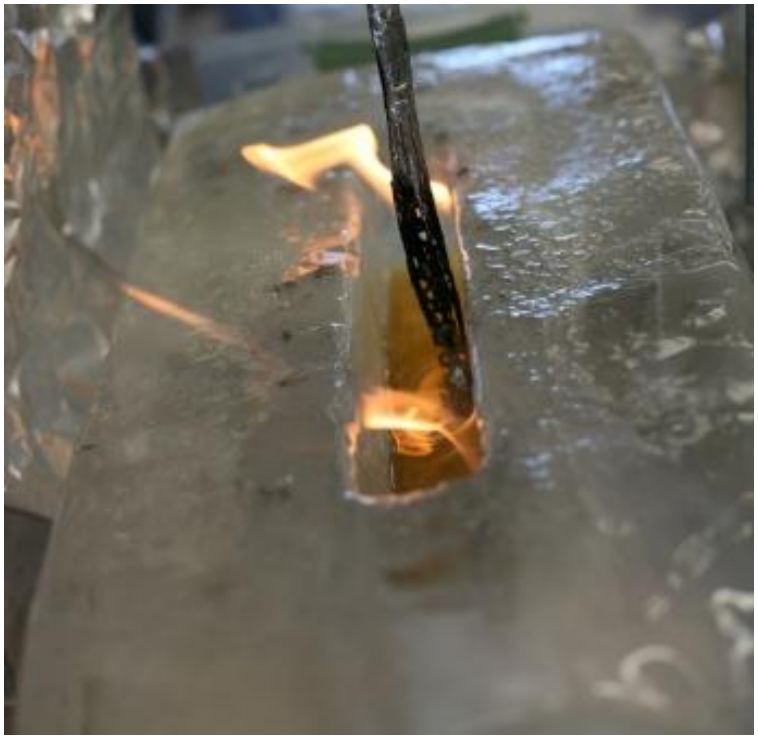

Figure A.23: 4 cm Trial 2: Zone 1 Close-up

Figure A.24: 4 cm Trial 2: Zone 2 Close-up

Figure A.25: The color version of Fig. 2.15

Figure A.26: 4 cm Trial 2: Cross Sectional View of Final Channel Width

Figure A.27: 4 cm Trial 2: Top View of Final Channel Width

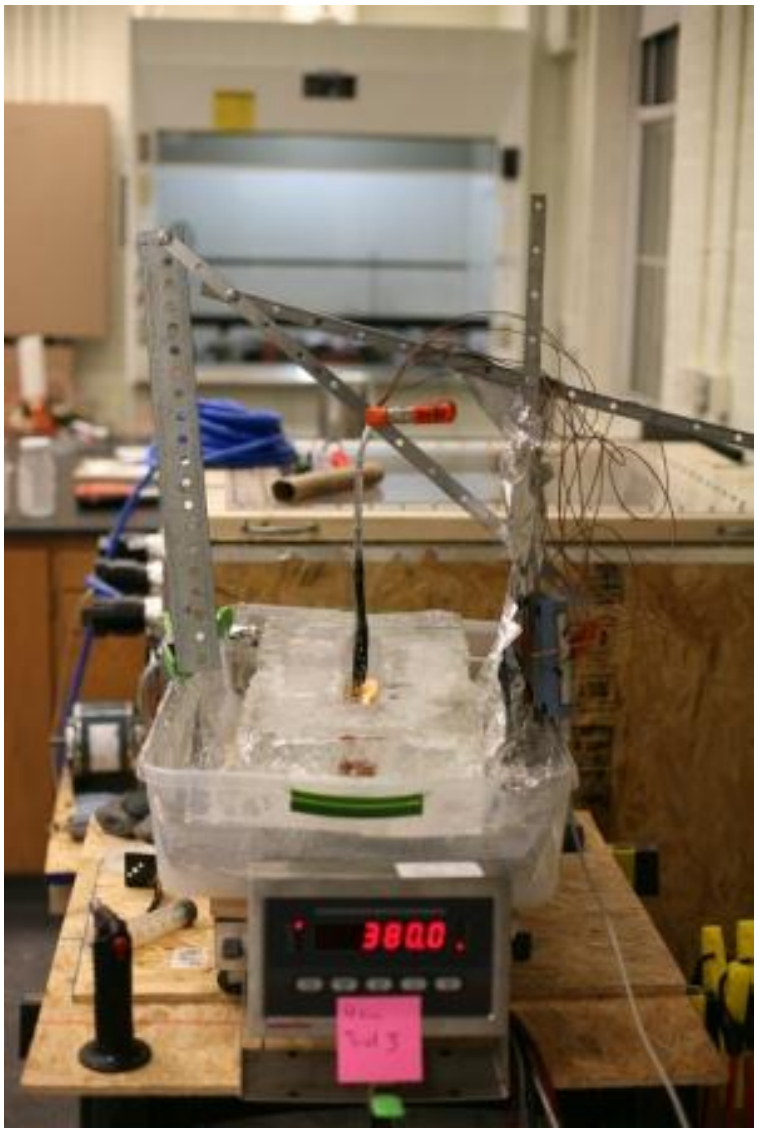

Figure A.28: 4 cm Trial 3: Zone 1 Burn

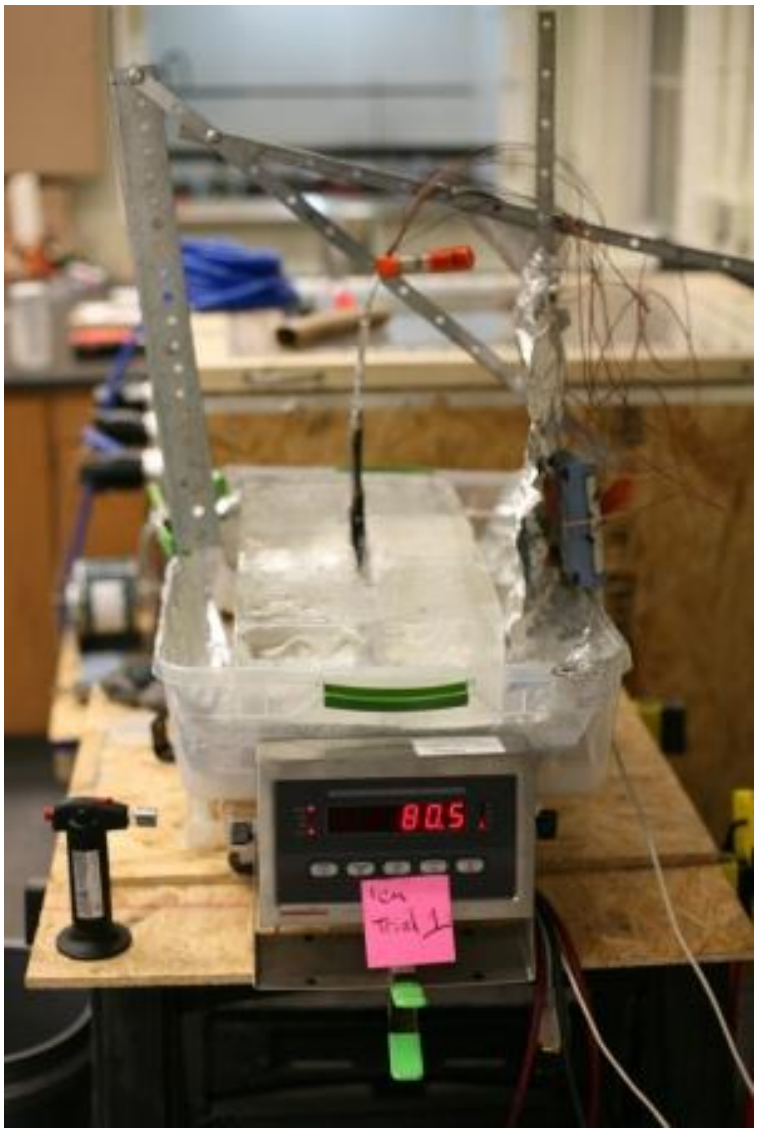

Figure A.29: 1 cm Trial 1: Preliminary Set-up

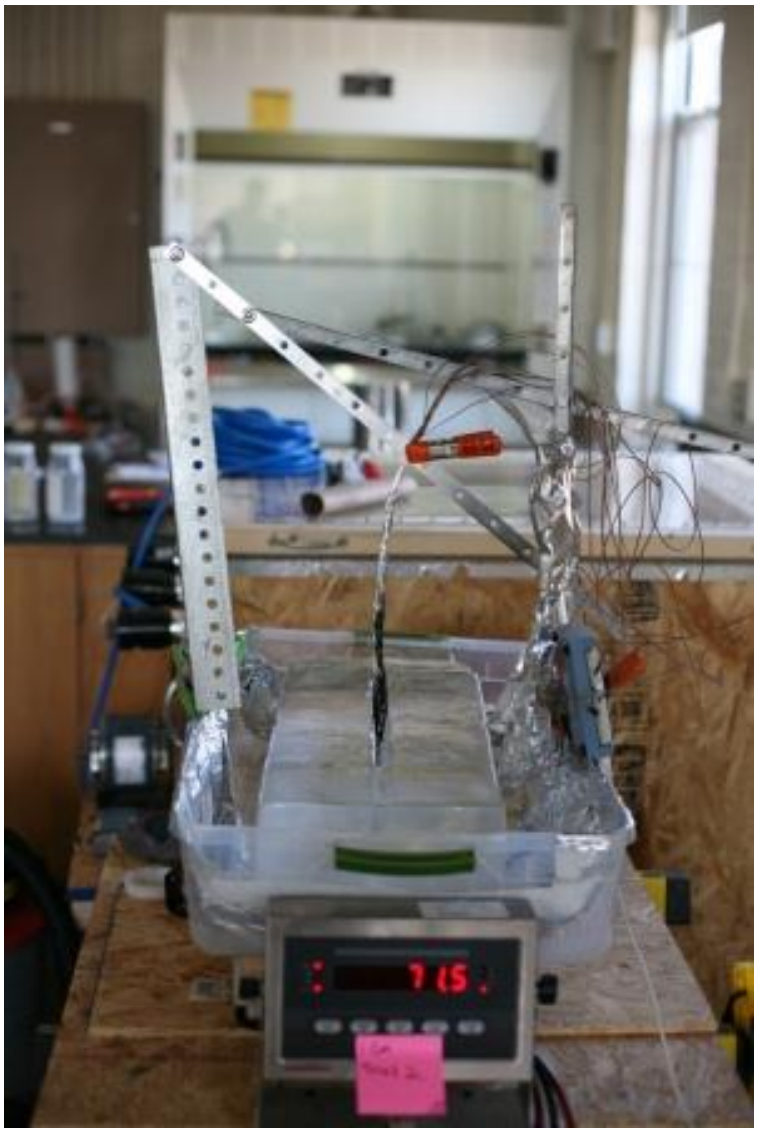

Figure A.30: 1 cm Trial 2; Preliminary Set-up

Figure A.31: Petroleum Ether Burn Spilling Over Edge

Appendix B

Spreading Appendix

The methodology of obtaining the various parameters used in the spreading equations are worked through here to provide the reader with some of the assumptions made during the analysis.

$$\begin{aligned} \Delta\rho &= \rho_c - \rho_a \\ &= 844 - 1.2 \\ &= 842.8 kg/m^3 \end{aligned} \tag{B.1}$$

$$\begin{aligned} \epsilon_a &= \frac{\Delta\rho}{\rho_a} \\ &= \frac{842.8}{1.2} \\ &= 702.33 \\ \epsilon_c &= \frac{\Delta\rho}{\rho_c} \\ &= \frac{842.8}{844} \\ &= 0.999 \end{aligned} \tag{B.2}$$

$$
\begin{aligned}
g'_a &= |\epsilon_a|\, g \\
&= 702.33 \times 9.81 \\
&= 6889.89 m/s^2 \\
g'_c &= |\epsilon_c|\, g \\
&= .999 \times 9.81 \\
&= 9.8 m/s^2
\end{aligned}
\tag{B.3}
$$

$$
\begin{aligned}
g' &= \frac{|\Delta\rho|}{max\,(\rho_a, \rho_c)} g \\
&= \frac{842.8}{844} \times 9.81 \\
&= 9.8 m/s^2
\end{aligned}
\tag{B.4}
$$

$$
\begin{aligned}
U &= \sqrt{g' h_0} \\
&= \sqrt{9.8 \times 0.3} \\
&= 0.54 m/s
\end{aligned}
\tag{B.5}
$$

h_0 is assumed to be the height of current upon reaching the first thermocouple (12 cm) at the given flow rate of 5.5 ml/s, 6.5 ml/s and 7.5 ml/s and an average transit time of 1.8 s, 2.0 s, and 4.0 s.

$$
\begin{aligned}
h_0 &= \frac{\dot{q} t}{A} \\
&= \frac{5.5 \times 1.8}{12} = 0.8 cm \\
&= \frac{6.5 \times 2.0}{24} = 0.5 cm \\
&= \frac{7.5 \times 4.0}{48} = 0.6 cm
\end{aligned}
\tag{B.6}
$$

$$
\begin{aligned}
Re = \frac{\sqrt{g'h_0}h_0}{\nu} & \\
&= \frac{\sqrt{9.8 \times 0.0.008}}{8.59 \times 10^{-4}} = 2.8 \\
&= \frac{\sqrt{9.8 \times 0.0.005}}{8.59 \times 10^{-4}} = 1.5 \\
&= \frac{\sqrt{9.8 \times 0.0.006}}{8.59 \times 10^{-4}} = 1.8
\end{aligned}
\tag{B.7}
$$

The following photographs are presented to give a different perspective to the work presented in the body of the document.

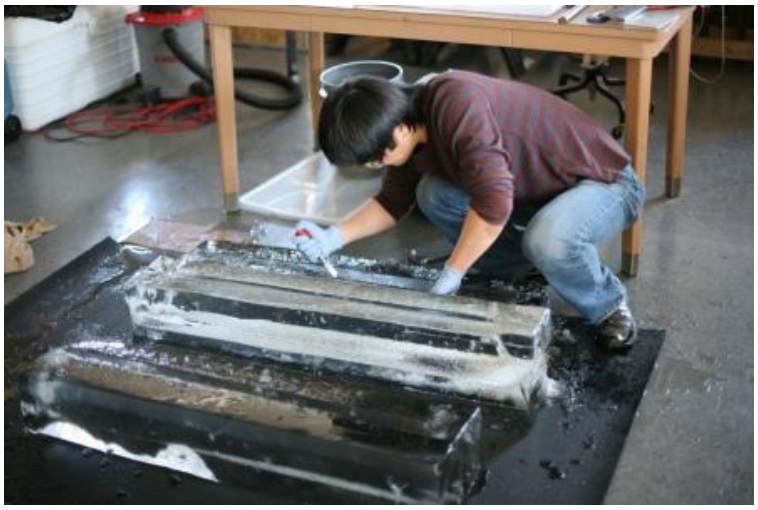

Figure B.1: Forming Ice Channel by Hand with Chisel

Figure B.2: 4 cm Channel Width Set-up

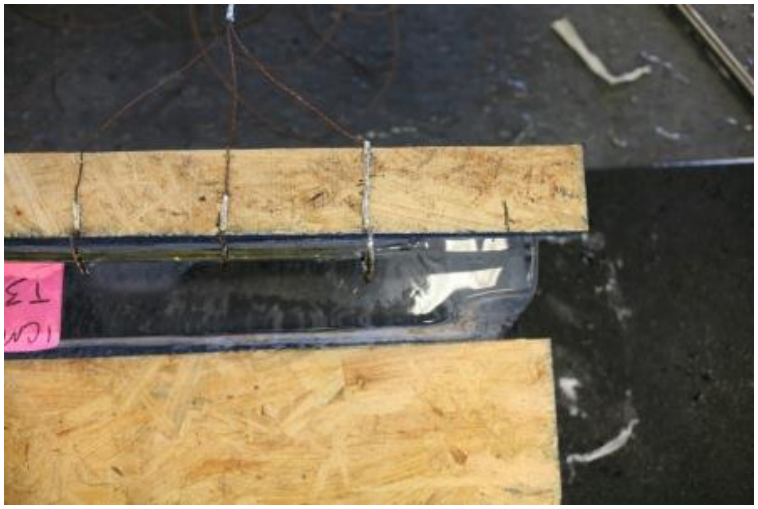

Figure B.3: 1 cm Channel Width Set-up

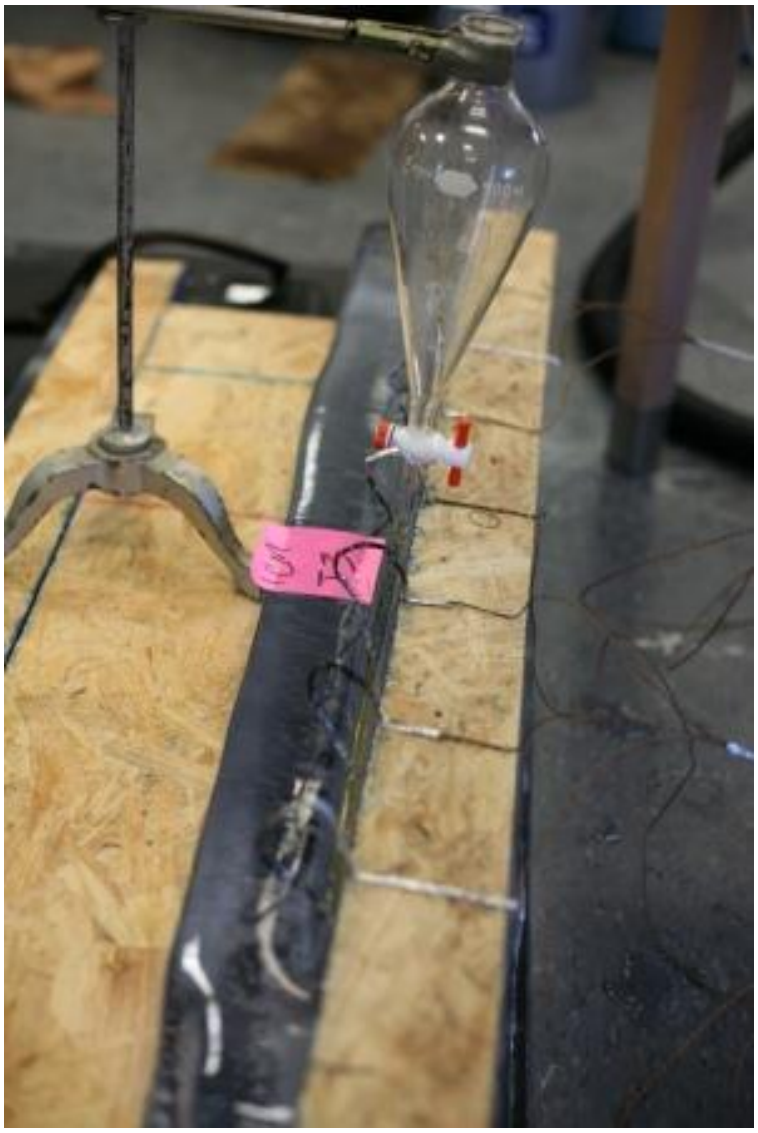

Figure B.4: 1 cm Trial 3 Experiment End

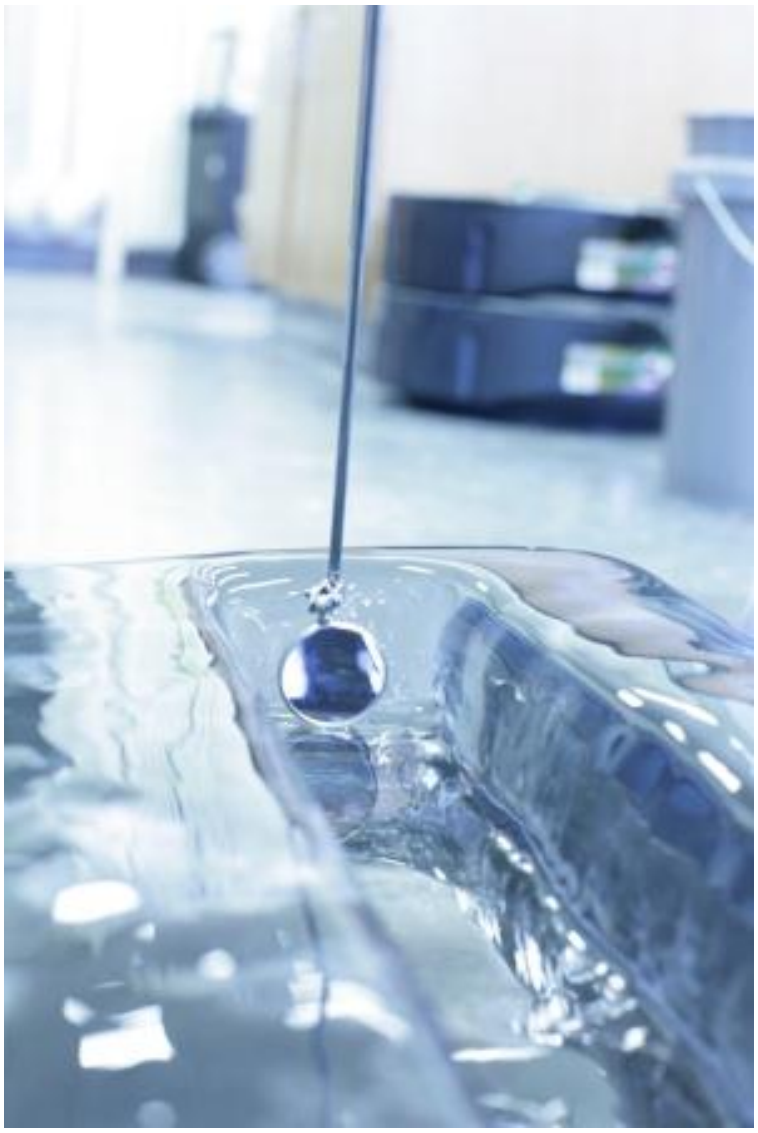

Figure B.5: 4 cm Channel Width: Attempts to photograph leading edge

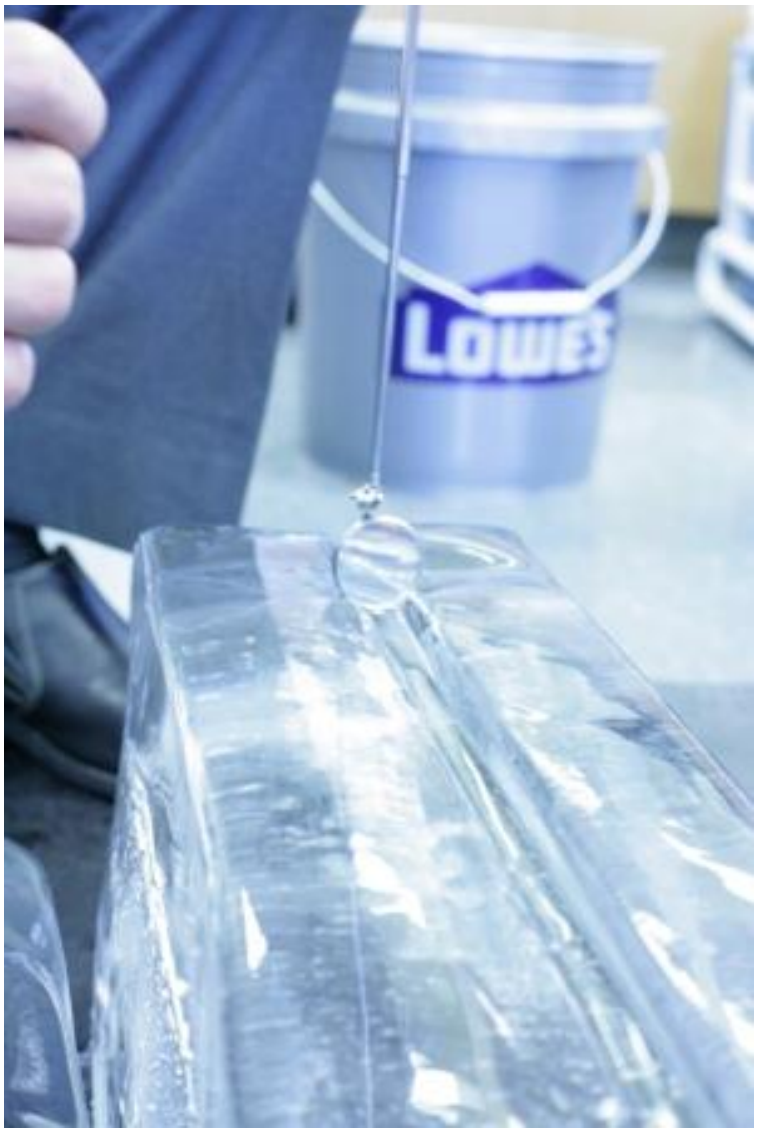

Figure B.6: 2 cm Channel Width: Attempts to photograph leading edge

Figure B.7: 2 cm Channel Width: Attempts to photograph leading edge failed